ISSN 0915-6410

ANNUAL REPORT OF THE NATIONAL ASTRONOMICAL OBSERVATORY OF JAPAN

Volume 1

Fiscal 1998

High-lights

First Light of Subaru Telescope

Norio KAIFU
(Subaru Telescope, Hilo, Hawaii · NAOJ)

In the eighth year of the nine-year construction project, Subaru Telescope, an 8.2-m effective aperture optical-infrared telescope, performed successful first light in December, 1998 and January, 1999. During the first light Subaru achieved the highest level of image quality and sensitivity among the existing telescopes, and also provided a number of preliminary scientific output. Test observations and fine adjustments of the system will continue for another one year toward the completion of the construction in 2000.

Figuring of the 8.3-m diameter ULE glass of the Subaru primary mirror was made in the Wampum factory of the Contraves Blashear Systems (CBS) near Pittsburgh. The final measurement of the surface accuracy of the primary mirror on the computer controlled active support system was made in the summer of 1998, which confirmed the remarkable high accuracy of the mirror surface (14 nano-meter rms). The primary mirror and mirror cell were then transported from Wampum to Hawaii via Mississippi Liver, Panama Canal and Honolulu, and arrived at the Mauna Kea summit on November 5, 1998. The mirror was then washed and coated with pure aluminum on November 8, and was mounted onto the telescope on December 2 (fig.1).

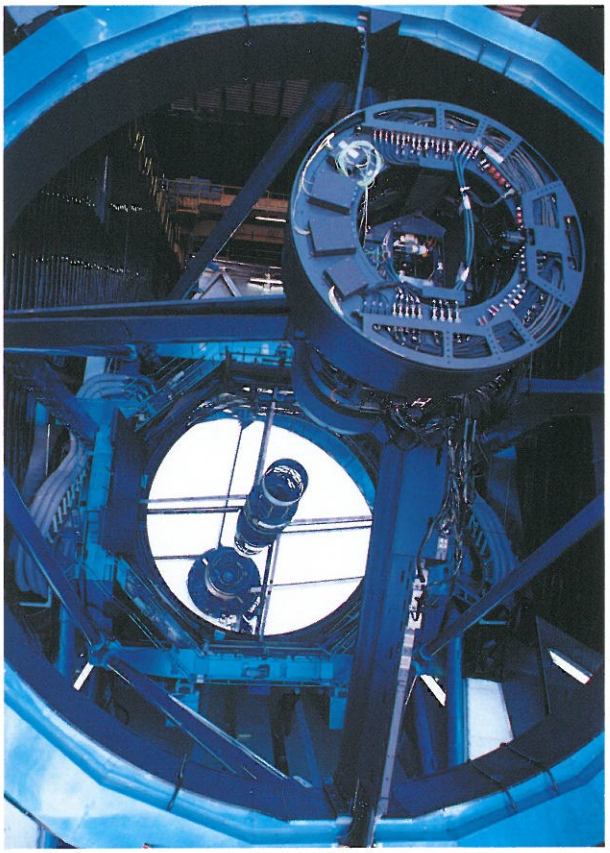

Fig.1: Subaru telescope at the time of FL. The blight area in the center of the telescope reflecting the sunlight is the 8.2m primary mirror. The black cylindrical structure at the center is a baffle for the Cassegrain and Nasmyth foci.

First Light (FL) is one of the most important events throughout the long construction period of Subaru telescope. Testing of the telescope imaging capability for the first time is mainly done to check and improve the optical and mechanical adjustments. FL also makes the start of the commissioning process by using the stellar light to verify the telescope as a complete operational system. Even though the telescope might not fully demonstrate its observational capabilities at the FL stage, it is an exciting event for the project in that the telescope produces observational data for the first time. We scheduled two events for FL: Engineering First Light (EFL) for testing optical alignment using simple cameras followed by Astronomical First Light (AFL) to confirm the performance using astronomical instruments.

During the AFL, the astronomical instruments used to demonstrate the performances were 'Cooled Infrared Specrograph and Camera for OHS' (CISCO) built by a group from Kyoto University, 'Subaru Prime Focus Camera' (Supreime Cam) built by a joint team from the University of Tokyo and the NAOJ and the 'High Vision Camera' (HVC) by NHK, a camera for high-quality color video images for public use. Above three observational instruments were equipped on the CIAX-3 instrument automatic exchanger and mounted to the Cassegrain focus one at a time. The CIAX-3 is one of the supporting systems for Subaru telescope to maximize the observing efficiency by allowing quick exchanges and mounting of the instruments to the Cassegrain focus.

The press conference held on January 27, 1999 was received exceptionally well throughout the world. Some of the pictures are presented here (fig.2, 3 and 4). The performances achieved during the FL are summarized below:

1. Achieved the highest level of angular resolution (0.3 arc-second stellar image during AFL, and 0.2 arc-second in February (fig.2) in the near infrared wavelength).
2. Acquired a large amount of premiere observational data reflecting the high observational capabilities of Subaru tele-

scope.

3. The spatial resolution of the Hubble Space Telescope surpasses the of Subaru telescope because of the absence of air turbulence that affects the image quality of ground-based telescopes. Subaru telescope, however, demonstrated its higher sensitivity for distant galaxies due to its large diameter. Subaru is expected to improve its angular resolution in the near future by the introduction of the adaptive optics and further refinements of the system.
4. Subsystems for the telescope, such as the computer controlled primary mirror support system, are all functioning satisfactorily.

Subaru telescope will be conducting various tests and tune-up of each sub-systems for even higher performance as a telescope, installing operation system software for astronomical observations and installing data analysis software for large amount of observation data. By the end of 1999 first-generation observational instruments will start arriving in Hawaii and the observational phase will start. Significant scientific results from Subaru telescope are expected to start flowing from this phase. The 'open use' phase will start in the later half of 2000. Researchers from Japan as well as from other countries will be accepted as observers for research with carefully selected observation program.

Reference

Kaifu, N.: 1998, *Proc. SPIE, Advanced Technology: Optical/IR Telescopes VI*, **3352**, 14-22

海部宣男：1999, 日本物理学会誌 (BUTSURI), vol.**54**. No.**4** (April 1999), 245-251

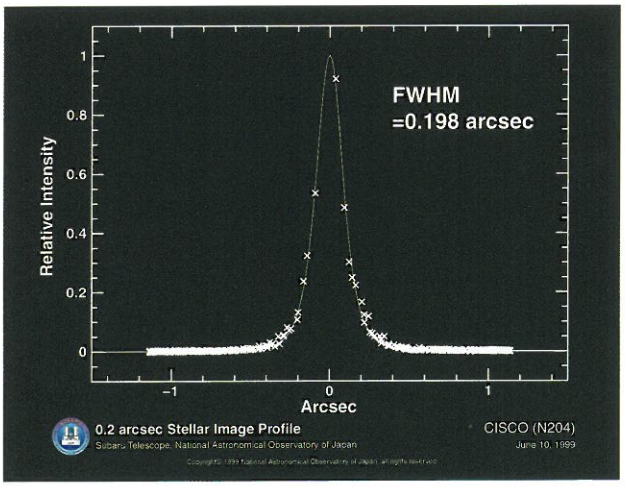

Fig.2: The Subaru telescope proved its high performance by achieving an angular resolution of 0.2 arc-seconds. Data acquired in February 1999, using Subaru and CISCO at a wavelength of 2 microns.

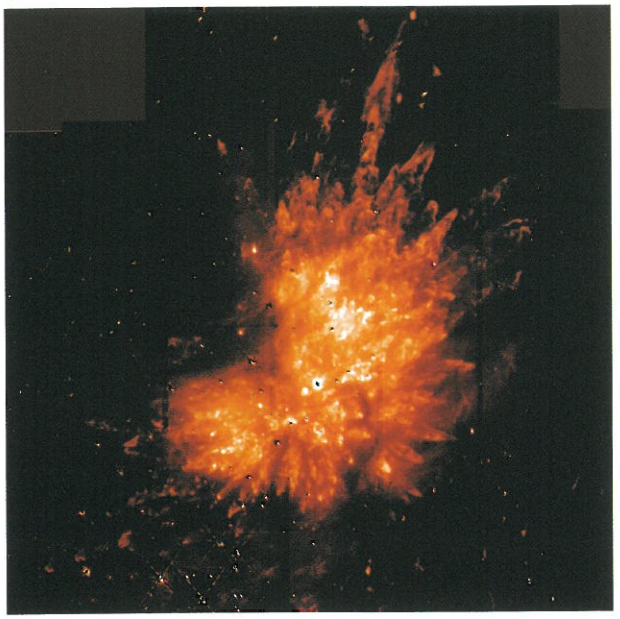

Fig.3: An infrared image of Irc @ in Orion Nebula created by hydrogen molecular emission lines (wavelength 2.12 μ m) with Subaru and CISCO. It shows a huge "sea-urchin" like feature formed by energetic flows from a very massive central proto-star. The observed area is 2 arc-min. Exposure time is 30 seconds.

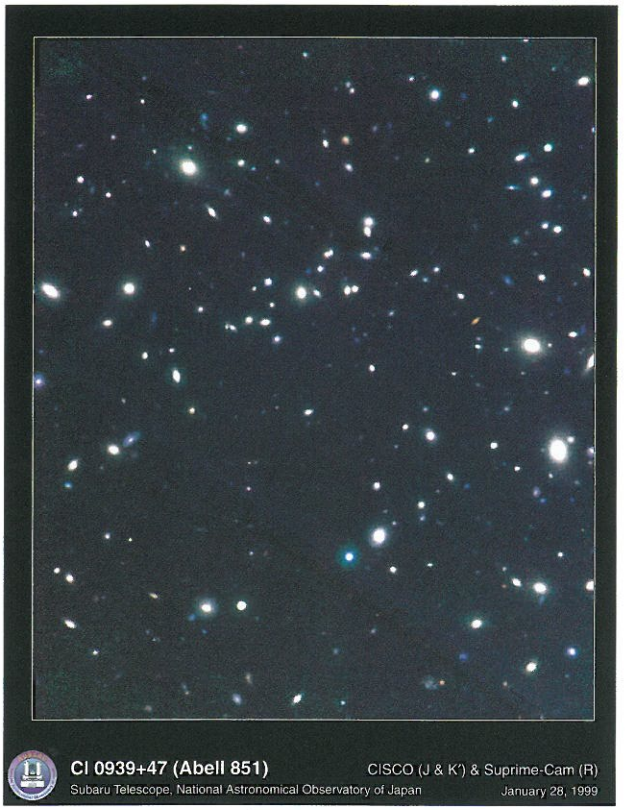

Fig.4: A cluster of Galaxies (CI0939+47, Abell851) located 5 billion light years away. This is a 3 colors synthesized picture with an optical image (blue) by the Suprime Cam and two near-infrared images (green and red) by the CISCO. The HST discovered many of the bluish faint galaxies seen here. In this image, however, we can also see a few red-colored galaxies (observed only in infrared wavelength) among the other galaxies. These were not seen in the HST image. The total exposure time for the 3 color image was 140 minutes.

Current Status of the TAMA 300 Gravitational-wave Detector

Masa-katsu FUJIMOTO, Seiji KAWAMURA, Masatake OHASHI, Toshitaka YAMAZAKI,
Ryutaro TAKAHASHI, Mitsuhiro FUKUSHIMA, Souichi TELADA
(Division of Astrometry and Celestial Meshanics · NAOJ)
Shuichi SATO
(Graduate University for Advanced Study)
Daisuke TATSUMI, Masaki ANDO, Shigeo NAGANO, Shinsuke TANIGUCHI, Atsushi SEKIYA
(University of Tokyo)
the TAMA Collaboration

TAMA 300 is the 300 m interferometric gravitational wave detector located at the Mitaka campus of National Astronomical Observatory. Setting up of the detector is almost finished and the first-stage operation of the detector will start soon.

The main results obtained in this academic year, as described below, are a stabilization of the light source which is composed of a 10 W laser and a 10 m ring cavity mode cleaner, a stable operation of a 300 m Fabry-Perot Michelson interferometer controlled in alignment and length, and a realization of power-recycled Fabry-Perot Michelson interferometer with relatively high recycling gain by the 20 m prototype.

Stabilization of the light source

A 10 W injection-locked LD-pumped Nd: YAG laser is used as the light source of TAMA 300. Light emitted from the laser transmits through the mode cleaner which is a ring cavity with 10 m armlength. The mode cleaner reduces the higher mode components as well as the beam jitter of the incident light. It also works as a reference in stabilizing the frequency of the light.

Combining the laser and the mode cleaner, 3.5 W light power was transmitted through the mode cleaner, which corresponded to 54 % transmittance of the mode cleaner. It fulfills the required 3 W output from the mode cleaner, taking various losses into account.

Frequency noise of the illuminating light spoils the sensitivity of the interferometer owing to inevitable asymmetry of the two arms of interferometer. The required frequency noise for TAMA 300 is $\delta\nu = 5 \times 10^{-7}\ \mathrm{Hz}/\sqrt{\mathrm{Hz}}$. Two stage stabilization scheme was designed in order to fulfill the requirement : the laser light is pre-stabilized up to $\delta\nu = 10^{-4}\ \mathrm{Hz}/\sqrt{\mathrm{Hz}}$ by using the mode cleaner as a reference at the first stage, and then the pre-stabilized light is further stabilized by using the 300 m Fabry-Perot cavity as a reference. Frequency stability of $\delta\nu = 2 \times 10^{-4}\ \mathrm{Hz}/\sqrt{\mathrm{Hz}}$ was attained by the pre-stabilization scheme.

Intensity noise also spoils the sensitivity owing to inevitable offset of the operating point of the interferometer. The required relative intensity noise for TAMA 300 is $\delta I/I = 1 \times 10^{-8}/\sqrt{\mathrm{Hz}}$. Intensity stabilization by combined use of an electro-optic modulator and a polarized beam-splitter resulted nearly required value $\delta I/I = 2 \times 10^{-8}/\sqrt{\mathrm{Hz}}$.

Long-term and stable control of the 300 m interferometer

Optical components of an interferometeric gravitational wave detector are suspended like pendulumns. They are al-

Fig.1 One of the two 300 m vacuum pipes installed in the tunnel. Laser beams travel back and forth inside of them.

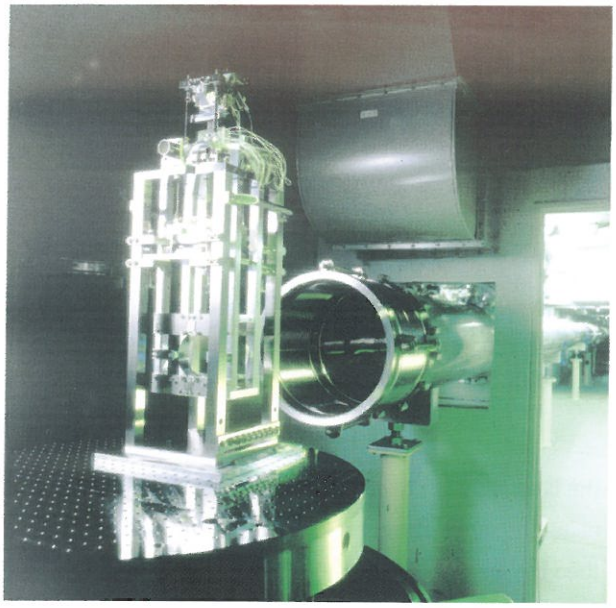

Fig.2 Suspension system for the mirror installed in the end vacuum chamber.

ways shaked by seismic vibration. Thus, we have to control the motion of the mirrors to keep the interferometer at an operational point.

In pararell to the above-mentioned light source experiment, we tried to operate the 300 m interferometer for a long time by using the same control configuration as the final one of the TAMA detector. In this experiment we used 700 mW Nd: YAG laser as a simple light source. We could operate the interferometer for 5 hours long. This is the first demonstration of operation of a Fabry-Perot Michelson interferometer with fully suspended optics under its alignment and length controlled. TAMA 300 is also the world largest interferometer in operation at present.

Refering to the performance of the interferometer, measured contrast was 97.3 $\pm$ 0.1 % and common mode rejection ratio (CMRR) of the interferometer was 90. These are close to the designed requirement that is 99 % for contrast and 100 for CMRR. The sensivity of the interferometer was about 10^{-15} m/$\sqrt{\text{Hz}}$. This is 2 $\times 10^{3}$ times worse than the designed sensitivity, 5 $\times$ 10^{-19} m/$\sqrt{\text{Hz}}$. However, it is not serious because we do not take care of the sensitivity in this experiment. The main purpose of this experiment is to control the interferometer stably for a long time.

Recycling of 20 m laser interferometer

The 20 m laser interferometer has been developed as a prototype of a full-scale laser interferometric gravitational-wave detector. It adopted IR light source, demonstrated the operation of optically recombined FP Michelson interferometer with dark fringe locking by using Shnupp (pre-modulation) method for the first time, and has been equipped with independently-suspended-mirror Mode Cleaner which transmits the phase modulated light. All of them are needed for a full configured detector. The other important technique to be investigated by the prototype is the power recycling.

The sensitivity curve of the interferometer is expected to be limited finally by some noise sources according to its frequency band. The shot noise limited sensitivity can be improved only by increasing the light power incident to the interferometer. So, the most important features which are required to recycling is to sufficiently enhance the incident light, that is, to obtain a high recycling gain. Of course, there have to be highly developed technique to control a complex system of coupled cavities, when recycling mirror is incorporated with interferometer. The expected maximum recycling gain is roughly approximated by "the inverse of total loss of the interferometer". For example, when the reflectivity of non-recycled interferometer is 90 %, total loss of it is 10 %, which leads maximum gain of 10.

In order to demonstrate high gain recycling on a prototype interferometer which have a order of 10 m length arms, poor quality and misalignment of mirrors which originate from the long arm cavities were serious problems. Long cavity means that the gaussian beam have a large mode radius. Laser beam whose diameter of typically 10 mm resonates inside arm cavity, so high quality mirrors were needed for such large area. Another one is a misalignment of the mirrors which were excited by seismic noise. These effects can degrade the reflectivity of the order of percent through extra coupling to higher order modes and poor interference efficiency at beam splitter, which become more serious for longer cavity.

It is standard to fabricate high quality mirrors for IR light by coating dielectric multi-layer with ion-beam-sputtering (IBS). Ultra-high quality optics have been developed by the group of ILS at University of Electro-communications. Total loss of mirror (including absorption, scattering and diffrac-

tion) of 1.5ppm was measured by tabletop experiment using fine beam of ~ 100 um diameter, which is still world record as an evaluation of optics with reliable errors. Same measurement was performed on a 20 m long cavity for thick laser beam to succeed to evaluate total loss for such wide area for the first time. Measured qualities of the cavity were finesse of 25000, storage time of 1 msec and total loss of 28 ppm /optic. These are sufficiently high qualities, satisfying the requirement of TAMA 300, 50 ppm / optic, with which recycling gain of 20 can be expected without another optical losses.

By using these high-quality mirrors, the 20 m interferometer could be operated as a power-recycled Fabry-Perot Michelson interferometer with sufficiently high gain, more than 12. Furthermore, by engagiment of a wave-front sensing technique, the remaining gain fluctuation due to mirror misalignments was sufficiently suppressed and the recycling gain was enhanced owing to the improved contrast. This work demonstrared experimentally that a full-configured interferometer which is a complex of coupled cavities can be locked into the final operation state by using a proper optical and control system.

This project is supported by a Grant in Aid for Creative Basic Research of the Ministry of Education, Science, Sports and Culture.

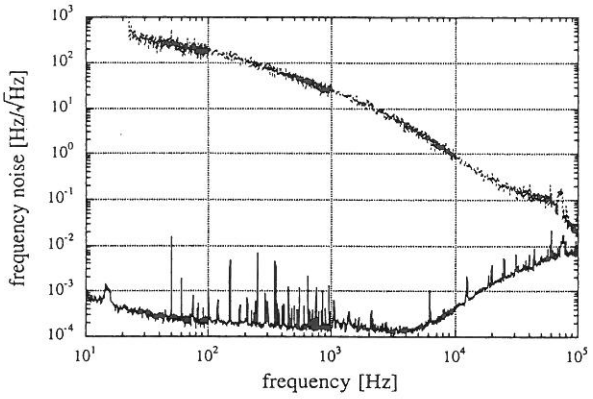

Fig.3 Frequency noise spectral density of the 10 W laser. The lower curve corresponds to the noise stabilized by using the 10 m mode cleaner as a reference, and the upper one shows the noise

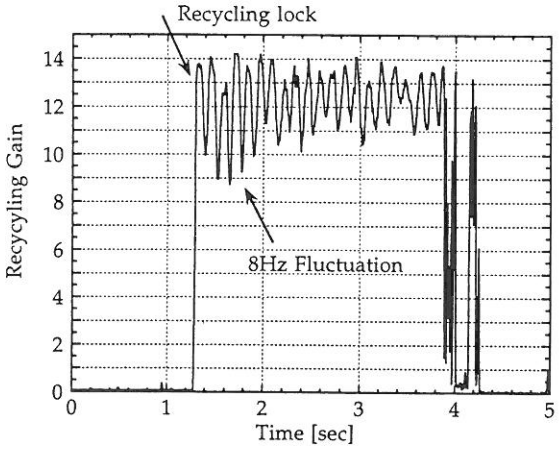

Fig.4 Recycling gain achieved by the 20 m prototype interferometer.

FTS Measurements of Millimeter and Submillimeter-wave Atmospheric Opacity at Pampa la Bola

Satoki MATSUSHITA
(Graduate University for Advanced Studies)
Hiroshi MATSUO
(Cosmic Radio Observing Facities of Nobeyama Radio Observatory · NAOJ)

The measurement of millimeter and submillimeter-wave (150 — 1500 GHz or 2 mm — 200 μm) atmospheric opacity spectra at Pampa la Bola site (Atacama desert of Northern Chile, 4800 m altitude; the prospective site for the Large Millimeter and Submillimeter Array [LMSA]) has been performed in winter season of 1997 and 1998 using a Fourier transform spectrometer (FTS). We obtained high transmission spectra, showing up to ~ 67 % transmission at submillimeter-wave windows (fig 1; black line). We also identified supra-terahertz windows (located around 1035 GHz, 1350 GHz, and 1500 GHz). Correlations between 220 GHz and submillimeter-wave opacities were derived, and proportional coefficients of about 20 in the submillimeter windows (650 GHz and 850 GHz windows) were obtained. Combined with a statistical study of the 225 GHz opacity data of the Chajnantor site (7 km apart from Pampa la Bola), it is estimated that submillimeter-wave observations can be done with zenith opacity less than 1.0 for about 50 % of the winter season. This is more than 50 % as better as in Mauna Kea, Hawaii.

We performed radiative transfer calculations using the model ATM (*Atmospheric Transmission at Microwaves*; Pardo and Cernicharo 1999) to fit the spectra. As can be seen in the figure, the model fits very well the observed spectrum (fig 1; red line). The fit results on precipitable water vapor column above the site indicate only 0.252 mm.

These results indicate that the Pampa la Bola — Chajnantor area is one of the best site for the submillimeter observations in terms of atmospheric opacity conditions.

References

Matsuo, H., Sakamoto, A., and Matsushita, S.: 1998, *Publ. Astron. Soc. Japan*, **50**, 359
Matsuo, H., Sakamoto, A., and Matsushita, S.: 1998, *Proc. SPIE*, **3357**, 626
Matsushita, S., Matsuo, H., Pardo, and Radford :1999, *Publ. Astron.Soc. Japan*, submitted

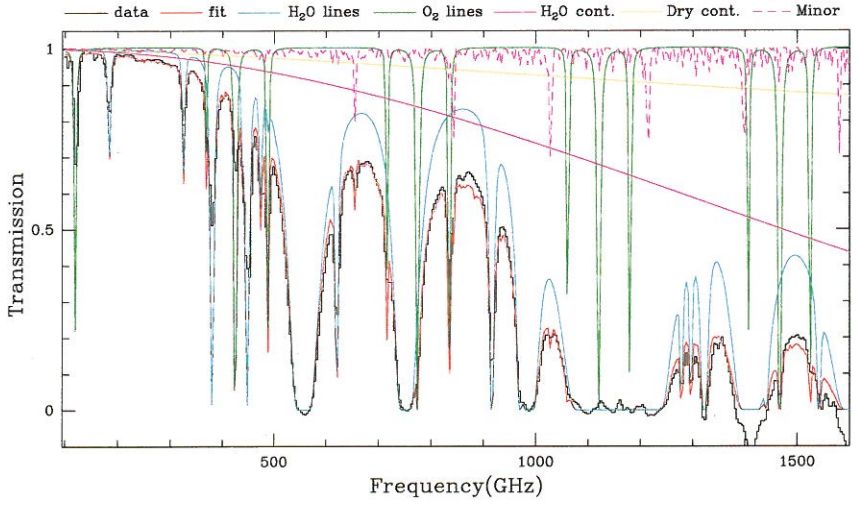

Fig.1 An atmospheric transmission spectrum and a theoretical radiative transfer calculation result. *Black line:* Observed spectrum. *Red line:* The best fitted radiative transfer model of the observed spectrum. This fitting is composed of absorptions indicated below. *Blue line:* Water vapor absorption lines. *Green line:* O_2 absorption lines. *Purple solid line:* Water vapor continuum absorption. *Yellow line:* dry air continuum absorption. *Purple dashed line:* Minor gas absorption lines.

Mt. Fuji Submillimeter-wave Telescope

Ken-ichi TATEMATSU, Takashi NOGUCHI
(Division of Radio Astronomy·NAOJ)
Satoshi YAMAMOTO, Yutaro SEKIMOTO, Mt. Fuji Submillimeter-wave Telescope Group
(University of Tokyo)

The submillimeter (submm) region, which is radio wave having a wavelength shorter than 1 mm, has been regard as one of the frontiers in observational astronomy. The submm region contains two atomic carbon (CI) lines, high-excitation rotational-transition lines of various molecular species, the red-shifted ionized carbon (CII) line from distant galaxies, which are of great interest in today's astronomy. Furthermore, the bulk of the dust thermal emission from the protostellar condensation, protoplanetary disk, and proto-galaxy is emitted in the submm region. Because absorption due to water vapor is very serious for the submm observations, the ground-based submm observatory should be constructed at sites higher than 3,000 m above sea level. In Japan, the summit of Mt. Fuji, which is the highest mountain in Japan, was thought to be one of the limited candidate sites for submm observations. By measuring with a 220 GHz radiometer, Sekimoto et al. found that the sky opacity at Mt. Fuji is good enough for submm observations [1]. We have started to construct the Mt. Fuji submm Telescope since 1995. The purposes of the telescope are to study the formation process of the molecular cloud, the physics of the photo-dissociation region, and the chemical evolution of the molecular cloud, through a large-scale survey observation of the CI lines in the submm region.

The main dish of the Mt. Fuji submm Telescope has a diameter of 1.2 m, and is enclosed in a 3-m diameter radome [2]. The altitude of the telescope is 3,700 m above sea level. Even at the summit of Mt. Fuji, the best observing season is limited in the winter time (Nov. — March), so the telescope is controlled remotely via satellite communication.

The telescope was first assembled in the Nobeyama Radio Observatory in 1997 June for test operation. In 1997 December, our group detected CO (J = 3 — 2) line at 345-GHz from Orion KL, which is the first submm astronomical observation in Japan. During 1998 January — March, various molecular clouds have been mapped in CO (J = 3 — 2) line. In 1998 July, the telescope was installed at the summit of Mt. Fuji by a helicopter. In 1998 September, our group detected CI (1—0) at 492 GHz for the first time in Japan.

Since 1998 October, we are mapping various molecular clouds, including the Orion A cloud and the Taurus molecular cloud, by observing 492-GHz CI and 345-GHz CO (J=3-2) simultaneously through remote operation. As a result, we found that atomic carbon is abundant in the early evolutionary stage of the interstellar cloud. The physical and chemical evolution of the cloud are being made clearer.

For the Mt. Fuji Telescope, Nobeyama Radio Observatory

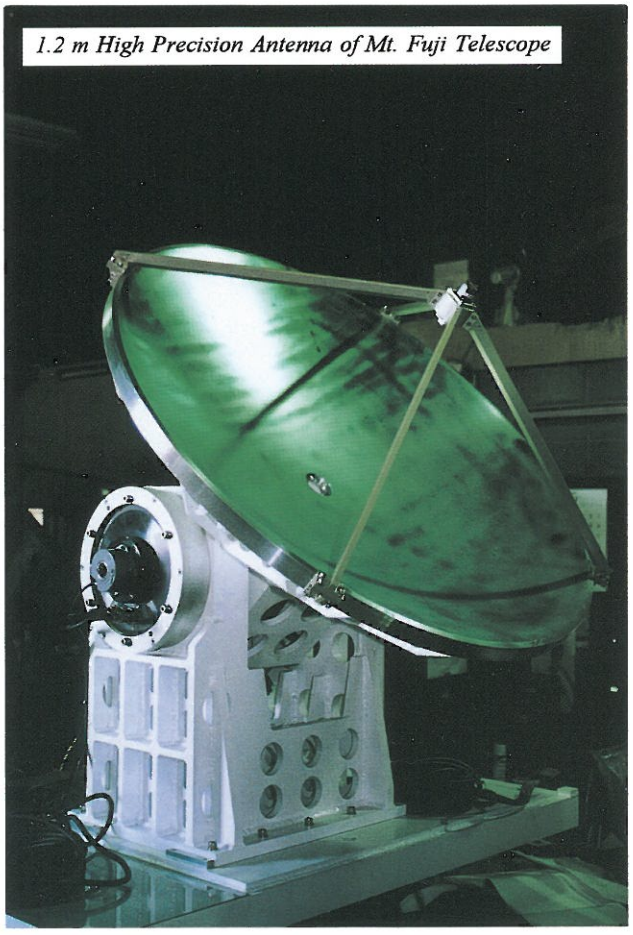

Figure1 1.2m High Precision Antenna of Mt. Fuji Telescope

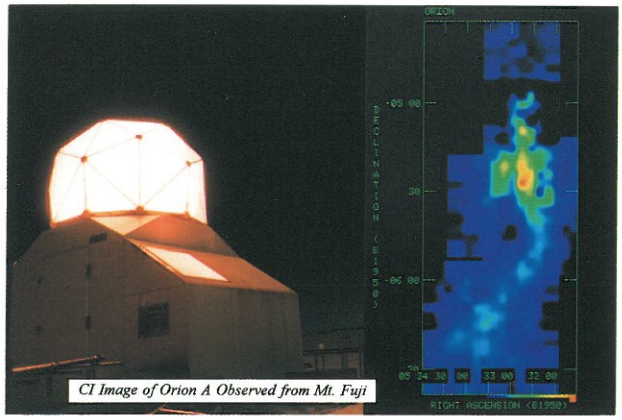

Figure2 CI Image of orion A Observed from Mt. Fuji

Figure3 Installation of the Mt Fuji submm Telescope by a helicopyer

developed the superconductor junction for the receivers (Noguchi and Shi), the submm receiver system, the telescope control software, remote operation via satellite communication, and the overall system test during the Nobeyama test operation. We plan to develop a receiver system for 809-GHz CI line, which is the next target for the Mt Fuji. Telescope,and to establish a high-efficiency observing method including the On-the-Fly mapping observation.

The Mt. Fuji submm Telescope project is carried out as a joint project of RESCEU of University of Tokyo, Nobeyama Radio Observatory of NAOJ, etc.

Reference

[1] Sekimoto, Y., Yoshida, H., Hirota, T., Takano, Y., Furuyama, E., Yamamoto, S., Saito, S., Ozeki, H., Inatani, J., Oh-ishi, M., Cardiasmenos, A.G., and Hensel, S.L.: 1996, *International Journal of Infrared and Millimeter Waves*, **17**(7), 1263-1284

[2] Sekimoto, Y., Yamamoto, S., Yoshida, H., Habara, H., Arikawa, Y., Hirota, T., Ikeda, M., Maezawa, H., Saito, S., Ozeki, H., Fujiwara, H. Inatani, J., Oh-ishi, M., Tatematsu, K., Miyazawa, K., Yang, J., snd Shiki, S.: 1997, in Diffuse Infrared Radiation and the IRTS., *ASP Conf Ser*, eds., H. Okuda, T. Matsumoto, and T. Rollig, **124**, 310-313

Development of HIDES, a High Dispersion Echelle Spectrograph for the 188 cm Reflector of Okayama Astrophysical Observatory

Hideyuki IZUMIURA, Hisashi KOYANAO, Kenshi YANAGISAWA, Takafumi OKADA
Michitoshi YOSHIDA, Yasuhiro SHIMIZU, Etsuji WATANABE, Fumihiro URAGUCHI
Yuji NORIMOTO, Shin-ichiro OKUMURA, Hideo MAEHARA
(Okayama Astrophysical Observatory · NAOJ)
Seiji MASUDA
(Kyoto Univ.)

Our new HIgh Dispersion Echelle Spectrograph (HIDES) of which construction started in fiscal year 1997 has succeeded in receiving the light from celestial objects at last (see flgures below).

HIDES is a spectrograph designed and developed for the use at the coude focus of the 188 cm reflector of Okayama Astrophysical Observatory, NAOJ. Its spectral resolution is three times higher than that of the current coude spectrograph for a given slit width. It also surpasses the current spectrograph at the simultaneous wavelength coverage by an order of magnitude. HIDES is designed to observe light in the wavelength range from 360 to 900 nm, and to achieve a resolution of 50,000 for a projected slit width of 1.0″ .

HIDES consists of a slit unit, calibration lamps, a collimator mirror (these three components are common with the current spectrograph), a filter wheel with order cutting filters, an echelle grating, two order-separating cross-disperser gratings, a camera optics, a CCD camera, and the control system. The echelle grating is fixed to a particular position. The CCD camera is designed to use a mosaic of two CCDs of 2K × 4K pixels (currently only one chip is available). As to the cross-disperser gratings one is used for blue region (below 450 nm) and the other for red region (above 450 nm). They can be interchanged in a few minutes. With the red cross-disperser and mosaiced CCDs HIDES gives a wavelength coverage of 200 nm at one exposure. The choice of a lens system for the camera optics enables to use large formatted CCDs without giving rise to vignetting of the incident beam.

HIDES is designed to reach a spectral resolution above 100,000. During a test observing run in the end of March 1999, it was indeed confirmed that the resolution was just above 100,000 in any part of the spectra of the calibration lamp as well as of a bright celestial source obtained with the 2K× 4K CCD when the projected slit width was 0.38″ . The maximum resolution was found to be 160,000. HIDES is the first spectrograph that can work regularly at a resolution around 100,000 for the 188 cm reflector. Now the read-out noise of the CCD is 4.5 electron. On the basis of the test observing run HIDES is expected to produce spectra with S/N greater than 10 for a point source of 12th magnitude after one hour exposure in the 400 - 700 nm wavelength range when the resolution is set to 70,000.

We will improve the user-interface, refine the temperature control of the coude room, and proceed the mosaicing and evaluation of the CCDs. Phased opening of HIDES to common use observations will start in year 2000. Further information on HIDES can be found at http://www.oao.nao.ac.jp/instruments/hides.

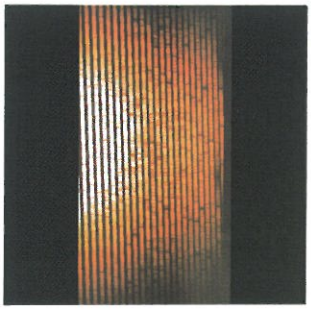

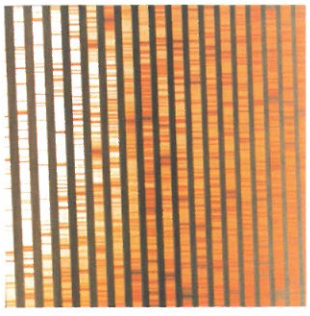

Left) A spectrum of the moon light from 395 - 467 nm recorded on a 2K×4K CCD from EEV. Resolution ($\lambda/\triangle\lambda$) achieved is 100,000 here. The dispersion directions of the echelle and cross-disperser gratings are vertical and horizontal, respectively. The lower-right corner corresponds to the shortest wavelenght. The blue cross-disperser was used and the slit length was 7.9″ . Echelle dispersion orders from 144 to 121 are seen. Free spectral ranges in this wavelength region are shorter than a half of the CCD vertical length. Thus, absorption lines on a certain order in the upper-half area are also seen on the adjacent lower order in the lower-half area. Right) A close up of the central part of the spectrum shown left. Echelle dispersion orders from 142 to 124 are shown. The vertical span is 27Å at the rightmost and 30Å at the leftmost. The horizontal span is about 580Å.

Development of Mitaka Optical/IR Array (MIRA): Observation of Apparent Diameter of Aldebaran (α Tau) and Fringe Tracking Experiment with MIRA-I.1

Jun NISHIKAWA, Yasuo TORII
(Division of Optical and Infrared Astronomy · NAOJ)
Yoshihiro MACHIDA
(University of Tokyo)
Koh-ich SATO
(Division of Earth Rotation · NAOJ)
Toshio FUKUSHIMA
(Public Relations Center · NAOJ)
Masanoori YOSHIZAWA, Shunsaku SUZUKI, Ko MATSUDA, Koh-ichi KUBO, Hikaru IWASHITA
(Division of Astrometry and Celestial Mechanics · NAOJ)
Yukihiro HONMA, Yuji KUBOTA, Zenichi NEMOTO
(Hosei University)

One of the most fundamental requirements in modern astronomy is the observation with a high spatial resolution to see fine structures of astronomical objects. It is well known that the spatial resolution of a single telescope is limited to the order of λ/D by diffraction, where λ is the wavelength of observation and D the diameter of the telescope aperture. The interferometry is a primary technique to realize a high spatial resolution in astronomical observations by using a set of element telescopes of relatively small sizes. The electromagnetic wave from each of the element telescopes is transmitted to one place to be combined, and when combined properly the interferometry provides us a higher spatial resolution than acquired with a single element telescope alone.

Under the project code MIRA, our group is advancing the project to develop a long-baseline optical/IR interferometer for astrometry and high-resolution imaging. The scientific goal of the project is to open a new field of optical astronomy in the researches of high-resolution stellar astrophysics, circum-stellar or circumquasar disks, and galactic dynamics. From a technical view-point, on the other hand, it is also important for us to acquire as much of the technical know-how as possible through the progress of the project, because we are required to bring our technical ability higher up to level indispensable for the development of a future large optical array and/or space interferometer.

The development of the first phase instrument, MIRA-I, was began in the year-end of 1995 at the Mitaka campus. By the end of March 1998, a 4m-baseline two-pupil interferometer aligned along the north-south direction and working at the optical red band (800 nm), had been almost completed for operation and detection of stellar fringes. MIRA-I consists of two coude telescopes and an optical bench in between where a number of optical components are arranged. The main optical components are, among others, a fine optical delay line, the tip-tilt mirrors and its quadrant sensors (four photon-counting Avaranche photo diodes = APD) for each telescope, the interference optics and a fringe sensor (APD) to measure the intensity of the interference fringes, the artificial lights (laser and white light), and so on [1]. The first detection of the stellar fringes with MIRA-I was achieved in June, 1998, for Vega (α Lyr) with 6cm aperture at the entrance of each telescope. This detection of the stellar fringes with an optical interferometer was the first one in Japan.

A part of the optical components of MIRA-I was replaced in July and August in order to improve the quality and efficiency of fringe detection (MIRA-I.1). Then, with the improved MIRA-I.1 we have performed a series of observations and experiments : the observations of the fringe visibilities of nine stars, the determination of the baseline vector, the determination of the apparent diameter of Aldebaran [Fig. 1], the fringe tracking experiments [Fig. 2], the measurements of the powers of atmospheric fluctuations of the angle of arrival, and the esti-

mation of the limiting magnitude reachable with MIRA-I.1 at the Mitaka campus. Thus, by the end of March, 1999, when the operation of MIRA-I.1 was successfully terminated, we could acquire much know-how on optical interferometry [2].

Now, since April 1999 we have been in a second phase of the project where a two-element, long baseline (30 m) interferometer of 30 cm siderostat aperture, called MIRA-I.2 [3], is scheduled for construction within two years. MIRA-I.2 will be one of the several modern long-baseline optical/IR interferometers operated in the world when completed.

References

[1] Machida, Y., Nishikawa, J., Sato, K., Fukushima, T., Yoshizawa, M., Honma, Y., Torii, Y., Matsuda, K., Kubo, K., Ohashi, M., Suzuki, S., and Iwashita, H.: 1998, *Proc. SPIE*, **3350**, 202-211.

[2] Nishikawa, J., and et al.: 1999, to be submitted to *Publ. Astron. Soc. Japan.*

[3] Sato, K., Nishikawa, J., Yoshizawa, M., Fukushima, T., Machida, Y., Honma, Y., Kuwabara, T., Suzuki, S., Torii, Y., Kubo, K., Matsuda, K., and Iwashita, H.: 1998, *Proc. SPIE*, **3350**, 212-217.

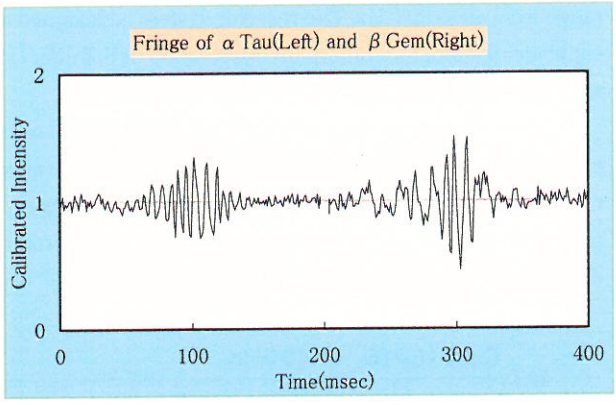

Fig. 1 Shown are the observed interference fringes of αTau, a star of large apparent diameter, and βGem, a star of small apparent diameter. The amplitudes of the observed fringes vary as a function of the apparent diameter of the observing stars with smaller amplitude for a larger apparent diameter. From our present observations, the apparent diameter of αTau is found to be about 20 milliarcsec.

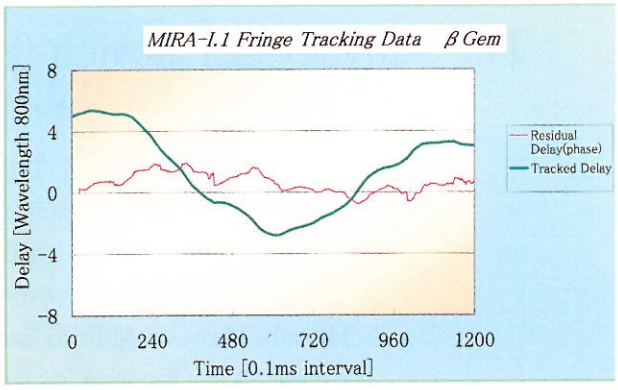

Fig. 2 The tracking trail of the fast delay-line and the residuals of the tracked delay with respect to the actual optical-path delay during the fringe tracking operation. The rapid variation of the optical-path delay due to the atmospheric turbulence is largely absorbed by the real-time counter-movement of the fast delay-line (PZT) which is under a feedback-control by using the measured phase of the central fringe. While the central fringe is kept under the control in the tracking system, the measurements of the amplitude and phase of the fringe are made continually. Thus the efficiency of the observations is increased greatly.

The Sunyaev-Zel' dovich (S-Z) Effect Observation Program using the Nobeyama 45-m Telescope

Masato Tsuboi, Takeshi Ohno, Atsushi Miyazaki
(Ibaraki University)
Takashi Kasuga
(Hosei University)
Hiroshi Matsuo, Akihiro Sakamoto, Nario Kuno, Suguru Noguchi
(Cosmic Radio Observing Facilities of Nobeyama Radio Observatory · NAOJ)

The Sunyaev-Zel' dovich (S-Z) effect (Sunyaev, Zel' dovich 1972) is caused by inverse Compton scattering of the cosmic microwave background radiation (CMB) with extremely hot gas in a cluster of galaxies. The cosmological significance of the effect is that the value of the Hubble constant can be estimated by combining the S-Z temperature decrement and the X-ray surface brightness of the hot gas. (e.g. Rephaeli 1995).

We observed the S-Z effect of a moderately distant cD cluster of galaxies, Abell 2218, at 36 GHz using a sharp beam of the Nobeyama 45-m telescope. The small beam size of the telescope is important because the S-Z temperature decrement is beam-diluted when the beam is larger than the angular size of the target clusters. This makes the observation easy in subtracting the emission from foreground, intracluster, and background point sources. The source contaminations are steeply decreased in the mm-wave range because the synchrotron emissions from contaminant sources drop steeply and the S-Z effect is essentially independent of the frequency up to about 100 GHz (Sunyaev, Zel'dovich, 1972).

We detected the Sunyaev-Zel' dovich effect in the mm-wave range toward Abell 2218 (Tsuboi et al. 1998). The antenna temperature decrement of the cosmic microwave background radiation (CMB) was measured to be $\triangle T_A^* = -0.52 \pm 0.15$ mK at the central peak position of X-ray emission in the cluster. Assuming that the hot gas in the cluster has isothermality, spherical symmetry, and the β-model density distribution, the Sunyaev-Zel' dovich effect is inferred to be $\triangle T_{0RJ} = -0.68 \pm 0.19$ mK at the Rayleigh-Jeans limit. A combination of this Sunyaev-Zel' dovich effect and X-ray surface brightness suggests that the Hubble constant is $H_0\ (q=0.5) = 54^{+51}_{-21}$ km s^{-1} Mpc^{-1}. In addition, this is the check of the reliability to observe S-Z effect using the Nobeyama 45-m telescope.

Our scientific goal is the reliable measurement of the Hubble constant based on sensitive mapping observations of S-Z effect toward many clusters. To realize these observations, we developed a 40-50 GHz array receiver (Ohno et al. 1998). Fig. 1 shows the array receiver installed on the focal plane platform of the Nobeyama 45-m telescope. This receiver has 6 feed horns and 6 SIS mixers. Their beams located at 2×3 grid with 90" interval on the sky make the mapping observation of S-Z effect easy. The mixer is operating in the frequency range from 40 to 50 GHz. The receiver system is designed as sophisticated tool for continuum observation of S-Z effect toward clusters of galaxies.

The S-Z temperature decrement was observed toward a distant cluster of galaxies, CL0016+16 at 43 GHz with the array receiver during the winter season of 1999. Fig. 2 shows the preliminary result of the distribution antenna temperature decrement. The S-Z temperature decrement was $\triangle T_A^* = -$

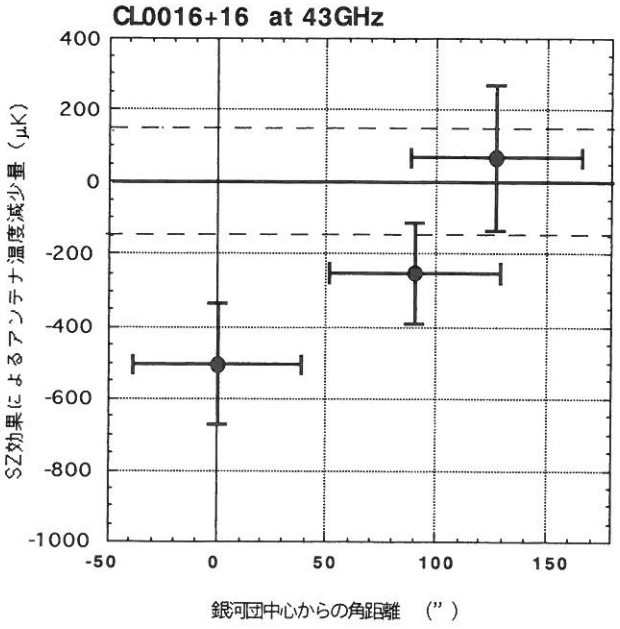

0.51 ± 0.15 mK at the center peak position of X-ray emission in the cluster.

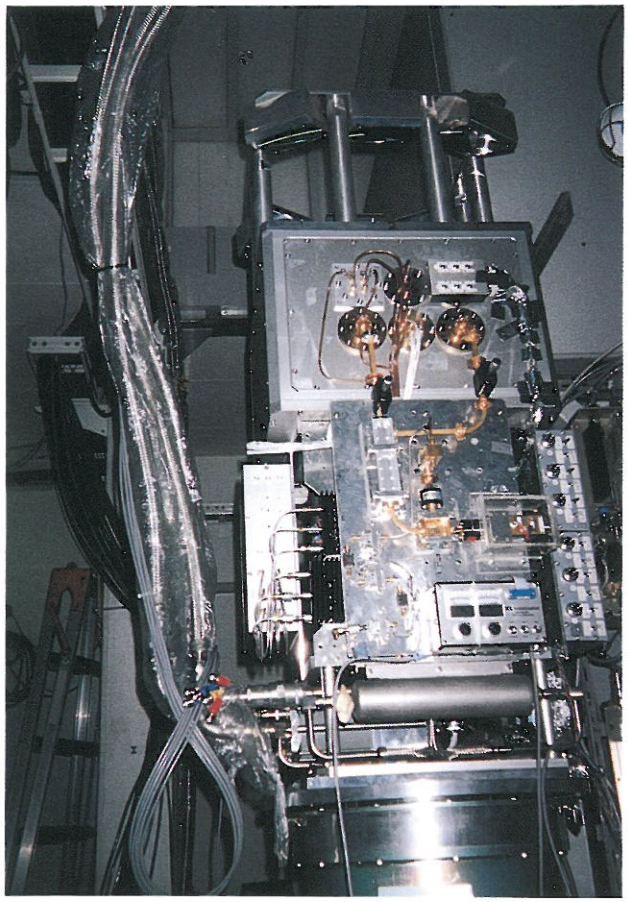

References

Ohno,T., Miyazaki,A, Tsuboi,M., Kasuga,T., Noguchi, T., and Sakamoto, A,; 1998, *Proc. SPIE,* **98**, 453

Rephaeli, Y.; 1995, *Annu. Rev. Astron. Astrophys.*, **33**, 541

Sunyaev, R. A., and Zeldovich, Y. B.; 1972, Comm. Astrophys. and Space Phys., *4*, 17,

Tsuboi, M., Miyazaki, A., Kasuga, T., Matuso, H., and Kuno, N.; 1998, *Publ. Astron. Soc. Japan*, **50**, 169

Submillimeter Polarimetry of Star-forming Regions with the SCUBA polarimeter

Motohide TAMURA
(Devision of Optical and Intrared Astronomy NAOJ)
Munetake MOMOSE
(Cosmic Radio Observing Facilities of Nobeyama Radio Observatory · NAOJ)
Junichi MORINO (University of Tokyo) A. CHRYSOSTOMOU, J. GREAVES, W. HOLLAND (Joint Astronomy Centre) J. H. HOUGH (University of Hertfordshire) A. G. MURRAY (QMW)

We have constructed a polarimeter for the submillimeter camera SCUBA at JCMT under UK-Japan collaboration. The SCUBA polarimeter has the following features: (1) imaging polarimetry is possible at wavelengths of 850/750 micron with 37 pixels (LW array), (2) imaging polarimetry is possible at 450/350 micron with 91 pixels (SW array), (3) simultaneous LW/SW polarimetry is possible with achromatic waveplates, (4) single-pixel polarimetry is possible at 1.1, 1.4, and 2 mm, (5) it has small instrumental polarization of about 1% except at 450 micron, (6) it has a high sensitivity with each pixel being almost 10 times better than the previous UKT14 system, (7) it has high spatial resolution of 7" at 450 micron and 13" at 850 micron, (8) it has a wide field of view of 2.3'.

We have conducted an imaging polarization survey of massive star forming regions including W3, W49A, W49 A North, NGC 7538 IRS1-3&11, Cep A, and GGD27 in order to reveal the magnetic field structure of the cloud cores. The regions are too dense to be studied with conventional optical polarimetry. The observed polarizations trace the magnetic field structure in the core regions because they are most likely due to polarized thermal emission from dust grains magnetically aligned in the core regions. The suggested magnetic fields show a locally coherent structure, but some complexity from regions to regions. In some cases, pinched fields or twisted fields are observed. These show various roles of magnetic fields in each of these massive star-forming regions.

Reference

Chrysostomou, A. et al.; 1998, Protostars and Planets IV

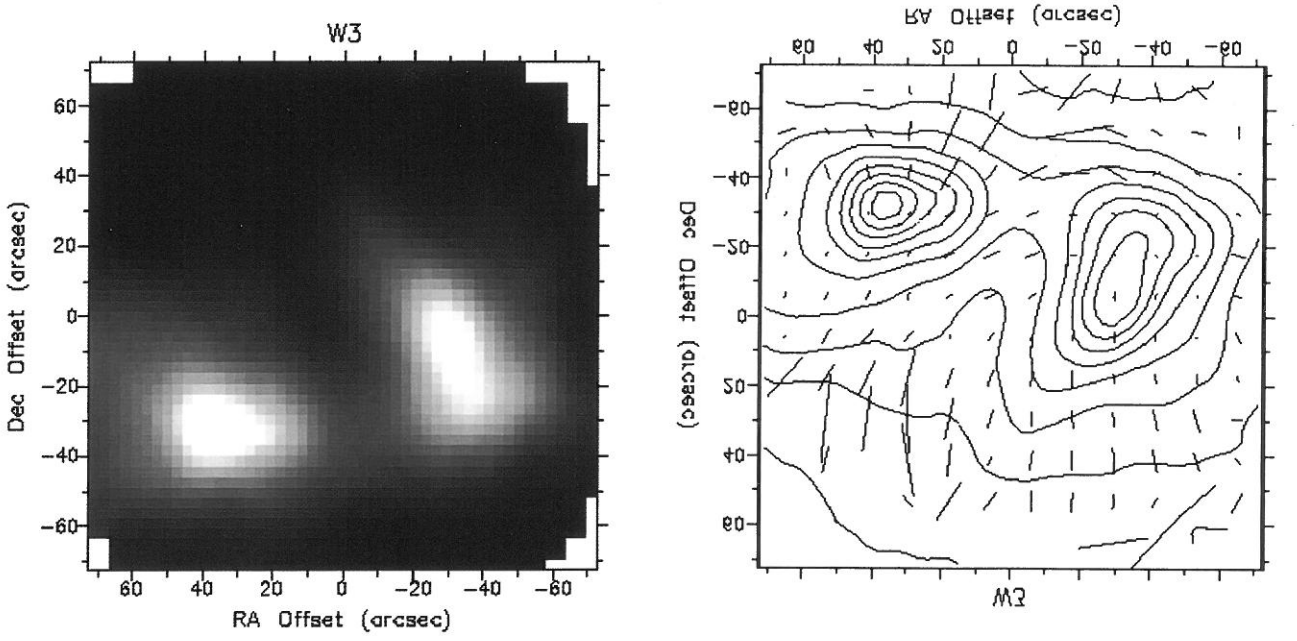

Fig. 1 850 micron surface brightness and magnetic field (polarization vectors rotated by 90°)

Stray-light Correction in Magnetograph Observation

J.C. Chae, H.S. Yun, Takashi SAKURAI, Kiyoshi ICHIMOTO
(Division of Solar Physics NAOJ)

At Mitaka, a video magnetograph (which is a part of the Solar Flare Telescope) has been in operation since 1992. The instrument uses a birefringent filter, which is made of calcite and quartz crystals whose total thickness is nearly 30 cm. This long optical path makes the stray-light level rather high. A single observation takes about 100 frames and accumulate them, and therefore the observation is susceptible to image motion during the integration. Those deteriorations in images can partly be recovered if the point spread function of the optical system is known. Here we used (1) the limb profile of the observed solar images, and (2) the observed power spectrum of the granulation pattern, to estimate the point spread function. A magnetogram corrected for the stray light in this way is shown in the right panel which should be compared with an original magnetogram on the left. In this example the corrected map shows a spatial resolution of about 2".

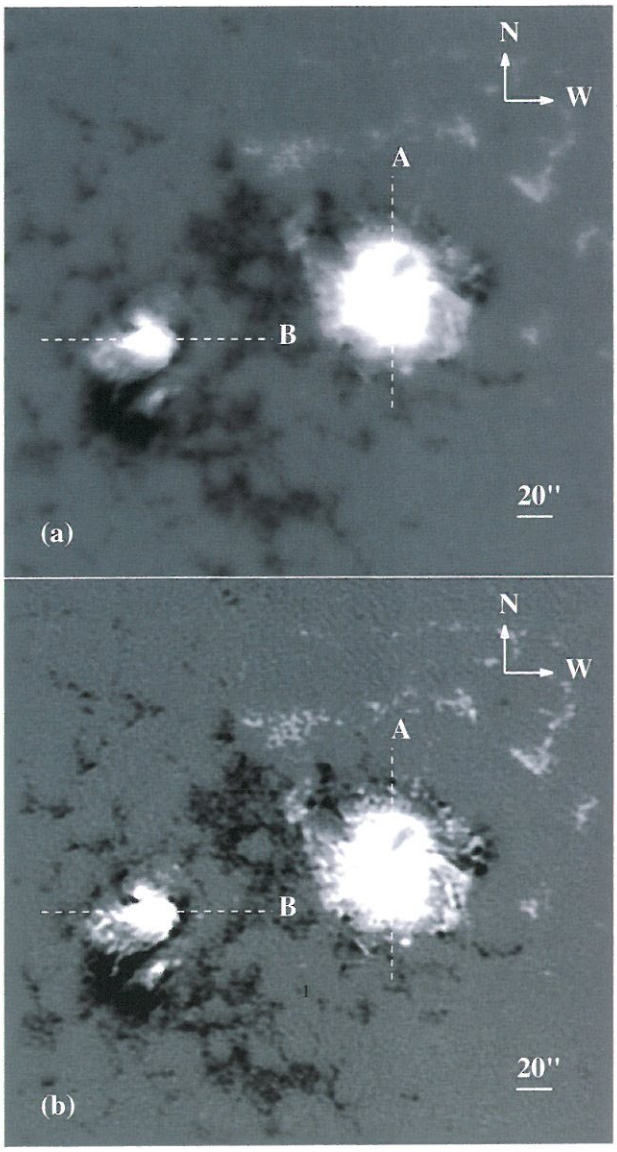

The original (top) and processed (bottom) magnetograms of a solar active region.

References

Chae, J.C. et al.;1998, *Solar Phys.*, **183**, 229 - 244,
Chae, J.C. et al.;1998, *Solar Phys.*, **183**, 245 - 261,

Simultaneous Spectrum of Sgr A* from 20 cm to 1 mm and the Nature of the Millimeter Excess

H. Falcke W.M. Goss Hiroshi. Matsuo
(MPIfR) (NRAO) (Cosmic Radio Observing Facilities of Nobeyama Radio Observatory · NAOJ)
P. Teuben J.-H. Zhao R. Zylka
(Univ. of Maryland) (Center for Astrophysics) (Institut fur Theoretische Astrophysik)

It is well known that the Galactic center radio source Sgr A* radiates strong synchrotron emission in radio frequencies, but their continuum spectrum in millimeter-wave region and their time variabilities are not known with reliability. Using Nobeyama 45 m, IRAM 30 m, BIMA and VLA, multiwavelength campaign observation have been carried out to reveal quasi-simultaneous spectrum of Sgr A* and their possible short time scale variabilities.

The Galactic center was observed on 1996 October 25-27 with VLA at 1.36, 1.44, 1.64, 4.85, 8.45, 14.9, 22.5 GHz, with BIMA at 93 GHz, with Nobeyama 45 m at 95 and 150 GHz, and with IRAM 30 m at 152 and 236 GHz. For single dish measurements at Nobeyama and IRAM, thermal emission component from surroundings of Sgr A* was subtracted using VLA 15 GHz image. Flux measurement at Nobeyama, IRAM and BIMA gives independent results but are consistent to each others. From these measurement the Sgr A* were not variable larger than 20 % within the measurement period. Their average spectrum is shown in figure 1. VLA observation shows marked break around 10 GHz, which are fit separately in the figure. Millimeter-wave emission is clearly in excess from extrapolation from the centimeter-wave measurements. There was multi epoch observations of Sgr A* which indicate the possible millimeter excess, but the current simultaneous measurements definitely revealed their existence.

The millimeter excess is compared with model calculation assuming synchrotron self-absorbed spectrum, which indicates the emission region have a radius of about 1.5×10^{12}cm. This size is comparable to the Schwarzschild radius ([4]0.8×10^{12}cm[4]) of 2.6×10^{6} $M_{\odot}$ blackhole. This would be interesting for millimeter-wave VLBI, since if the blockhole situate within the emitting region, the blackhole horizon could be imaged against the background of this millimeter-wave emission.

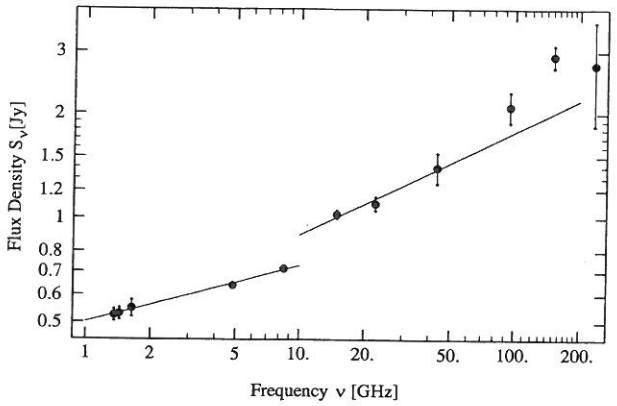

Fig. 1 The simultaneous spectrum of Sgr A* from 20 cm to 1 mm. Average spectrum during the measurement period is shown. Measurements at close frequencies are averaged on the plot. This shows measurement with the Nobeyama 45 m at 95 and 150 GHz was important to reveal the millimeter-wave excess.

References

Falcke, H., Goss, W.M., Matsuo, H., Teuben, P., Zhao, J.-H., and Zylka, R.: 1998, *Astrophys. J.*, **499**, 731.

High Angular Resolution Images with VLBI Space Observatory Programme (VSOP)

Makoto INOUE
(Division of Radio Astronomy · NAOJ)

Massive Black Hole and Jets

Very Long Baseline Interferometry (VLBI) has been developed to achieve high angular resolution in imaging the nuclear region of radio quasars and galaxies. VLBI observations of milli-arc-second (mas) scale structure revealed core-jet structure in the nuclear region, where a massive black hole presumably exists. Mass of billions of stars is concentrated in it, and gas around it is accreting. On the other hand, gas is accelerated close to the speed of light and emanated from the core. The size of black hole is almost the same order of the solar system, and the jets are generated within a parsec or a light year from the black hole. Some jets are ejected far from the black hole, up to millions of parsec well beyond the scale of parent galaxy, and jets are often seen as traveling faster than the light speed. Huge amount of energy is released around the black hole and violent phenomena we never know so far may happen.

Space VLBI VSOP and the satellite HALCA

The scale of sub parsec is, however, not easy to see by telescopes. Only VLBI has capability to image such violent regions, although it has not yet enough resolution. The angular resolution of interferometer increases with baseline length, or distance between a pair of telescopes. VLBI has, however, no more room to extend the baseline on the ground, as the baseline is already extended to the diameter of the Earth. Institute of Space and Astronautical Science (ISAS) initiated the VLBI Space Observatory Programme (VSOP) by close collaboration with NAOJ. The satellite, the Highly Advanced Laboratory for Communication and Astronomy (HALCA), attained the longest baseline of 30,000 km towards the ground radio telescopes, and is giving high angular resolution images of core-jet structures at 1.6 and 5 GHz. For cores, measurement of the brightness temperature is one of the key targets. A brightness temperature limit of 10^{12} K comes from incoherent synchrotron emission, and high brightness temperature sources test the Doppler boosting by the relativistic motion. While jets will show fine structures of knots, bending, etc. to give hints of jet propagation and collimation. The initial results are published, and images are seen in the ISAS web site (http://www.vsop.isas.ac.jp).

Reference

Hirabayashi, H. et al.: 1998, *Science*, **281**, 1825 — 1829.

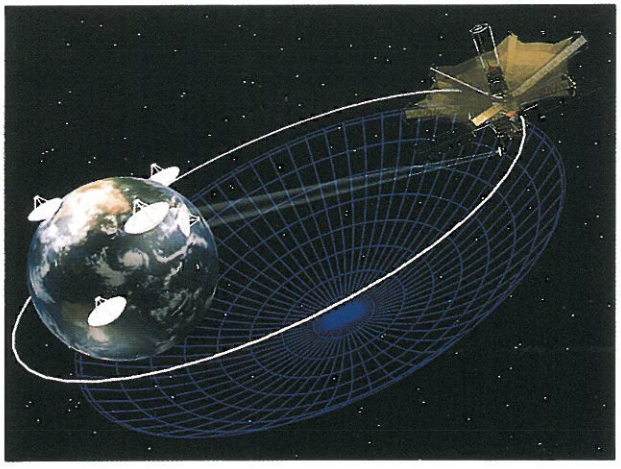

Magnetic Reconnection As the Origin of the Galactic-ridge X-ray Emission

Shun-ich TANUMA (University of Tokyo)
Taka-aki YOKOYAMA (Cosmic Radio Observing Facilities of Nobeyama Radio Observatory. NAOJ)
Tetsuhiro KUDOH, Kazunari SHIBATA (Division of Solar Physics NAOJ)

Abstract

Strong thermal X-ray emission is observed along Galactic plane (Galactic Ridge X-ray Emission, GRXE, Koyama et al. 1989). Origin of hot component is not known, while cool one is made of supernovae (Kaneda et al. 1997). We propose a possible mechanism to explain the origin (Tanuma et al. 1999). We solved two-dimensional resistive magnetohydrodynamicse quations numerically to examine the magnetic reconnection triggered by a supernova. The magnetic reconnection heats X-ray plasma in Galactic plane if it occurs in locally strong magnetic fields of 30μG. Heated plasma is confined by magnetic fields for a long time.

Numerical simulations

The initial condition is as follows: Temperature (0.8 keV, cool component) and total pressure are uniform everywhere. Gas pressure and density are uniformoutside the current sheet. Magnetic field is $B_0 = 30\ \mu$G ($\beta = 8\pi Pg/B_0^2 = 0.2$). We put a supernova.

Magnetic reconnection converts magnetic energy to thermal energy. Gas is heated to 7 keV, and confined by the magnetic field for $10^{5.5}$ yr. Most of thermal energy comes from magnetic energy, not from explosion. Required interval of reconnections (triggered by supernova, Parker instability, cosmic rays, turbulence etc.) is 10 ($\Delta\ E_{mag}/10^{51}$ erg) yr. The magnetic reconnection will explain X-rays from Galactic ridge, furthermore Galactic halo and clusters of galaxies.

Acknowledgements. The numerical computations were carried out on VPP300/16R and VX/4R at the National Astronomical Observatory of Japan.

References

Kaneda, H., Makishima, K., Yamauchi, S., Matsuzaki, K., and Yamasaki, N.; 1997, *Astrophys. J.*, **491**, 638

Koyama, K., Awaki, H., Kunieda, H., Takano, S., Tawara, Y., Yamauchi, S., Hatsukade, I., and Nagase, F.: 1989, *Nature*, **339**, 603

Tanuma, S, Yokoyama, T., Kudoh, T., Matsumoto, R.,Shibata, K., and Makishima, K. 1999, *Pubi. Astron. Soc. Japan*, **51**, 161

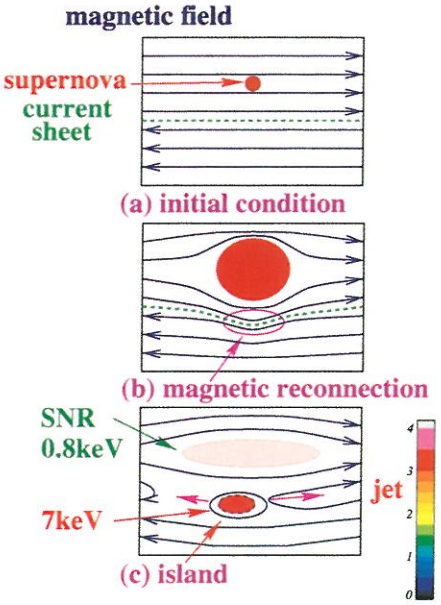

Fig.1 Our new Scenario of magnetic reconnection triggered by a supernova. Magnetic reconnection generates X-ray plasma.

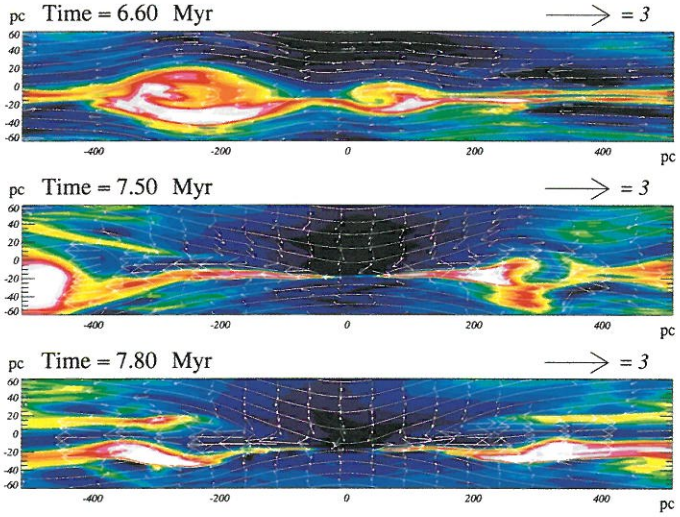

Fig.2 Time evolution of two-dimensional distribution of X-ray thermal flux. Initial magnetic field is $B = [Bo \tanh(y/20\ \mathrm{pc}), 0]$. The temperature and density are in the units of $n_0 = 5 \times 10^{-3}$ cm^{-3} and $kT_0 = 0.8$ keV. Supernova perturbs the current sheet. Magnetic reconnection heats gas by releasing magnetic energy.

Stellar Population of M31 Spiral Arm Around OB Association A24

Keiichi KODAIRA, (Director General · NAOJ)
Vladas VANSEVI (Visiting Professor · NAOJ)
Motohide TAMURA, (Division of Optical and infrared Astronony · NAOJ)
Satoshi MIYAZAKI (Advanced Technology Center · NAOJ)

A study on the stellar population of M31 spiral arm around OB association A24 was carried out based on the photometric data obtained from deep V and JHK imaging. The luminosity function was obtained for $-7 < M_{bol} < -3.5$ by applying the extinction correction corresponding to $A_V = 1$ and the bolometric correction BC_K as an empirical function of $(J-K)_0$. In comparing the observed color-luminosity diagrams with semi-theoretical isochrones modified for the dust-shell effects, we found that the prominent populations were a young component of $t < 30$ Myr with supergiants of $M_{bol} < -5$, an intermediate-age component of $t \sim 0.2 - 2.5$ Gyr with bright AGB stars of $-5 < M_{bol} < -4$, and an old component of $t > 5$ Gyr with AGB and RGB stars of $M_{bol} > -4$. The average star formation rate was estimated to be $\sim 1.8 \cdot 10^4\ m_\odot$/Myr and $\sim 0.7 \cdot 10^4\ m_\odot$/Myr per a deprojected disk area of 1 kpc^2 from the number density of B0V stars around $M_V = -4.0$ (age $\sim$ 10 Myr) and the number density of bright AGB stars around $M_{bol} = -4.3$ (age $\sim$1 Gyr), respectively. A study of the local variation in the V and the J and H luminosity functions revealed a kind of anticorrelation between the population of the young component and that of the intermediate-age component when subdomains of $\sim$ 100 pc scales were concerned. This finding suggests that the disk domain around the A24 area experienced a series of star formation episodes alternatively among different subdomains with a time scale of several spiral passage periods. Brief discussions are given about the interstellar extinction and about the lifetimes of bright AGB stars and the highly-red objects in the same area. (Abstract of reference 3)

Reference

1. Kodaira, K., Miyazaki, S., Vansevicius, V., Tamura, M., Tokunaga, A., and Kobayashi, N.: 1998a, *Astrophys. J. Supl.*, **118**, 177
2. Kodaira, K., Tamura, M., Vansevicius, V., and Miyazaki, S.: 1998b, *Astrophys. J.*, **500**, L133
3. Kodaira, K., Vansevicius, V., Tamura, M., and Miyazaki, S.: 1999, *Astrophys. J.*, **519**, No.1, in press

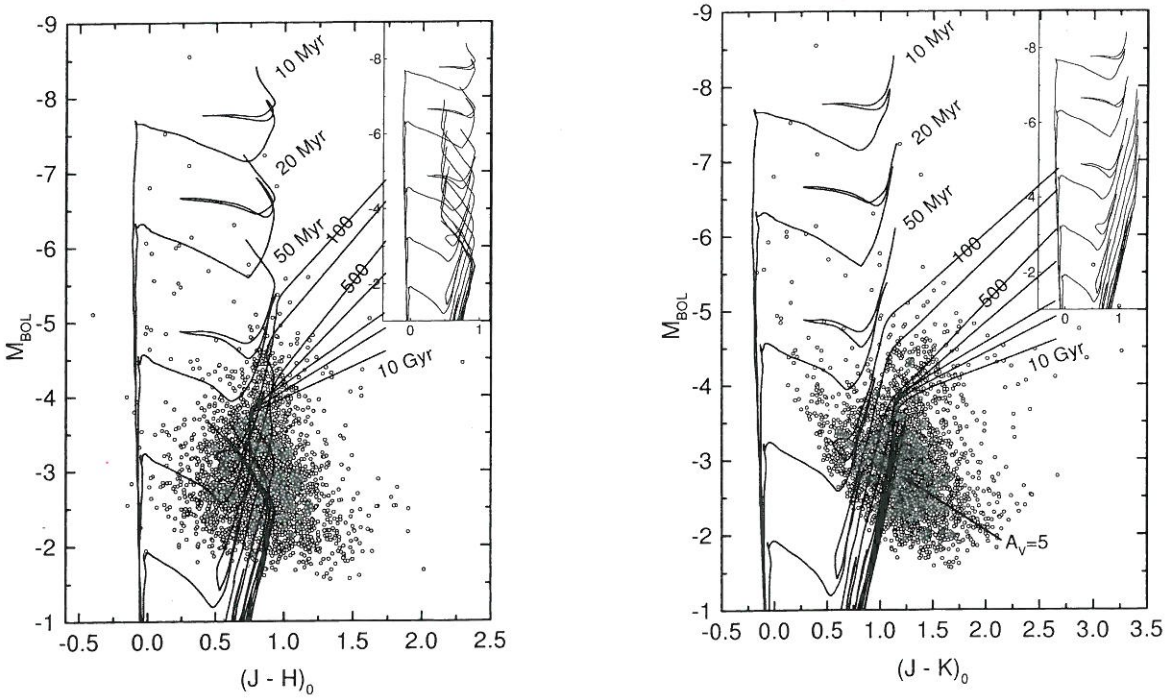

Color magnitude diagrams for stars in the 2' × 2' JHK field. The isochrones are those modified using dust-shell models. The ages of the unmarked isochrones are 1, 2, 5 Gyr. The oldest two cases are for Y=0.25 and Z=0.008, and the others are for Y=0.28 and Z=0.02. A dereddening vector for A_V = 5 is indicated according to the Galactic extinction law. Original isochrones of Padova 94 are shown in the insets.

High Resolution Imaging of the Infalling Gas around the Protostar L1551 IRS5

Munetake MOMOSE
(Grad. Univ. for Advanced Studies)
Nagayoshi OHASHI
(Academia Sinica Institute of Astronomy and Astrophysics, Taiwan)
Ryohei KAWABE, Takenori NAKANO
(Division of Radio Astronomy · NAOJ)
Masahiko HAYASHI
(Subaru Telescope Hawaii Facility · NAOJ)

T Tauri stars and their surrounding circumstellar disks grow by accretion of matter caused by dynamical infall of the protostellar envelopes. Recently, several observations of protostellar envelopes with millimeter arrays were made, providing strong evidence for infall in these envelopes. However, these observations were not able to reveal the internal structure of the envelope because of their insufficient angular resolution. To reveal the detailed structure of a protostellar envelope, we have made aperture synthesis $C^{18}O$ (1-0) observations of the nearby protostar L1551 IRS5 using the Nobeyama Millimeter Array (NMA) with higher angular resolution. Thanks to the high angular resolution (around 350 AU at the distance to IRS5), the detailed structure of the envelope has successfully been revealed as follows.

The left panel of the figure shows our observational results. The integrated intensity of the gas emission (contour) shows elongated structure in the direction perpendicular to the outflow, indicating the existence of a disklike envelope around the central star. The radius and mass of the disklike envelope are 1200 AU and 0.062 solar-mass. On the other hand, the mean-velocity distribution (color) shows two remarkable features. One is the velocity gradient along the minor axis in the outer part of the envelope: The blueshifted emission is located in the southwestern part while the redshifted emission is located in the northeastern part. The other is the velocity gradient near the star, which is nearly along the major axis. These features of the observed mean-velocity distribution can well be explained by the case in which the infall is dominant in the outer part while the rotation gets prominent in the inner part, as shown in the right panel. The analysis of position-velocity diagrams has revealed that the infall velocity in the outer part of the envelope is 0.5 km s^{-1} at r = 700 AU with a radial dependence of $r^{-0.5}$ while the rotational velocity, 0.24 km s^{-1} at the same radius, gets prominent at inner radii with a radial dependence of r^{-1}. This velocity field suggests that the gas in the envelope is infalling dynamically conserving the angular momentum.

The mass infall rate in the envelope is derive to be around 6×10^{-6} solar-mass per year from the mass and radius of the envelope and infall velocity. The velocity field in the envelope suggests that the rotational velocity gets equal to the infall velocity at r = 160 AU. Around this radius, it is expected that the dynamically infall motion shifts to the centrifugally-supported motion, giving natural scenario of the growth of the circumstellar disk.

Reference

Momose,M. et al.; 1998, *Astrophys. J.*, **504**, 314-333

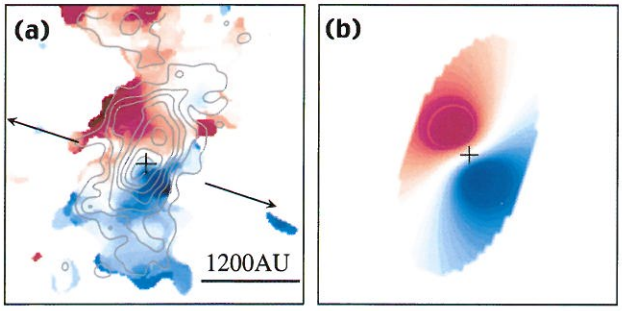

(a) The contour map shows the integrated intensity of the $C^{18}O$ (1-0) emission. The colar shows the mean-velocity distribution: The blue indicates the distribution of gas blueshifted from the systemic velocity while the red indicates that of redshifted gas. Deeper colors indicate greater velocity shifts. The arrow in this panel indicates the direction of outflow axis. (b) Expected mean-velocity distribution for the case where the infall is dominant in the outer part while the rotation gets prominent in the inner part. The cross in each panel indicates the stellar position.

Dense Molecular Gas Associated with the Circumnuclear Star Forming Ring in the Barred Spiral Galaxy NGC 6951

Kohtaro KOHNO, Ryohei KAWABE, B. VILA-VILARO
(Cosmic Radio Observing Facilities of Nobeyama Radio Observatory · NAOJ)

Observational studies of molecular gas in the Milky Way have clearly shown that stars are formed from dense cores of molecular clouds rather than their diffuse envelopes. It is therefore essential to study the properties of dense molecular gas in order to understand star formation in galaxies and particularly starburst phenomena. Here we present high resolution (3" - 5") observations of CO (1-0) and HCN (1-0) emission from the central region of the barred spiral galaxy NGC 6951, a host of type2 Seyfert nucleus, using the Nobeyama Millimeter Array and Nobeyama 45 m telescope. NGC 6951 is a barred spiral galaxy with a massive star forming ring of about 1 kpc diameter, and the circumnuclear star forming ring provides us with a unique opportunity to investigate the relationship between dense molecular medium and star formation.

Figure 1(a) and 1(b) show the comparison between CO, HCN, and Hα distributions. We find that most of the HCN emission is associated with the circumnuclear ring, where vigorous star formation occurs. The HCN to CO integrated intensity ratio in the brightness temperature scale, R(HCN/CO), is enhanced up to 0.16 - 0.18 in the star forming ring, as shown in Figure 1(c) and 1(d). The observed R(HCN/CO) value of 0.16 - 0.18 is higher than those in quiescent regions such as the Galactic disk ($\sim$ 0.02), and are comparable to those in the starburst regions of NGC 253 ($\sim$ 0.2).

The formation mechanism of dense molecular gas has been investigated. No significant enhancement of R(HCN/CO) is observed at the CO peaks, which are interpreted as orbit-crowding regions. This suggests that the shocks along the orbit crowding may not promote the formation of dense molecular gas. Instead, gravitational instability can account for the dense molecular gas formation because Toomre's Q value is below unity where R(HCN/CO) is enhanced.

The R(HCN/CO) toward the nucleus of NGC 6951, where type-2 Seyfert activity has been reported, is about 0.086. This ratio is similar to that in the central a few 100 pc region of the Milky Way, and quite different from other type-2 Seyferts such as NGC 1068 and M 51 where extremely high ratios, about 0.5, are observed.

Reference

Kohno, K., Kawabe, R., and Vila-Vilaro, B.; 1999, *Astrophys. J.*, **511**, 157

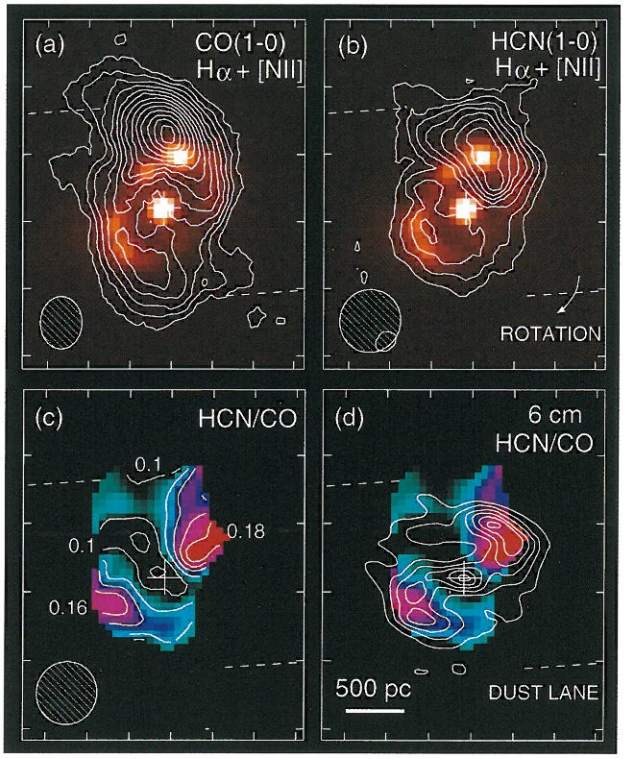

Figure 1. Integrated intensity maps of CO and HCN emission, and the comparison between molecular gas distribution and massive star formation. (a) CO (contour) vs Hα. (b) HCN (contour) vs Hα. The HCN emission spatially correlates better with the massive star forming regions than the CO emission. (c) Map of HCN/CO integrated intensity ratio, R(HCN/CO), in brightness temperature scale. (d) R(HCN/CO) vs 6 cm radio continuum (contour). R(HCN/CO) is enhanced (or the fraction of dense molecular gas) is enhanced at the massive star forming regions traced by radio continuum.

An Origin of Filamentary Structure in Molecular Clouds

Tomoya NAGAI
(University of Tokyo)
Shu-ichiro INUTSUKA Shoken M. MIYAMA
(Division of Theoretical Astrophysics · NAOJ)

The gravitational instability of a pressure-confined isothermal gas layer with uniform magnetic fields is investigated in the linear regime. We solve the eigenvalue problem for the growth rate of linear perturbations and obtain the dispersion relation and eigenfunctions.

The unperturbed state is an isothermal equilibrium layer. The unperturbed magnetic field lines are uniform and parallel to the mid-plane of the layer. For the layer with a thickness much larger than pressure scale height H, perturbations parallel to the magnetic fields grow faster than those perpendicular to the fields. Therefore, the layer fragments into filaments, and the direction of longitudinal axis of each filament is perpendicular to the magnetic field lines. On the other hand, the layer with a thickness much smaller than H fragments into filaments, and the direction of longitudinal axis of each filament is parallel to the magnetic field lines (Fig.1). We find that the critical half thickness of the layer of which the most unstable mode changes its character is $H/\sqrt{2}$ regardless of the strength of magnetic fields. Hence the isothermal layer confined by the external pressure that is larger than about 0.63 times the central pressure fragments into filamentary gas clouds threaded by magnetic fields parallel to them.

Fate of unstable layer is expected as Fig.2. If the external pressure is small, the layer fragments into filamentary clouds perpendicular to magnetic fields. The filamentary cloud only collapses toward the axis and perturbations do not grow much in the isothermal phase. That is, such a filamentary structure would be expected to fragment when the actual interstellar gas becomes non-isothermal and the collapse of the filament is decelerated. After that, it finally fragments into subclumps whose mass is about $0.1M_{\odot}$, if $T\simeq 10$ K. On the other hand, a filamentary cloud formed from the layer compressed by high external pressure is threaded by magnetic fields parallel to it. The magnetic fields reduce the maximum growth rate of instability. The filament may remain stable for a long time in comparison to the free fall time, and may not lead to star formation. The subsequent evolution might be through plasma drift and coalescence of the clouds.

Reference

Nagai,T., Inutsuka,S., and Miyama,S.M.: 1998, *Astrophys. J.* **506**, 306

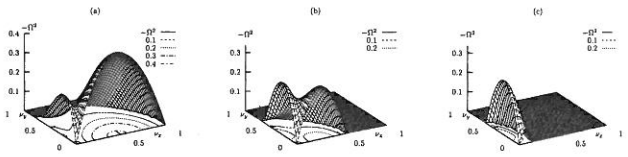

Fig. 1 The dispersion relation with $\mathbf{k}=(k_x,k_y)$ for the half thickness $z_b/H=$ (a)5.0, (b)$1/\sqrt{2}$, and (c)0.1. The strength of magnetic fields is $\alpha'=10.0$.

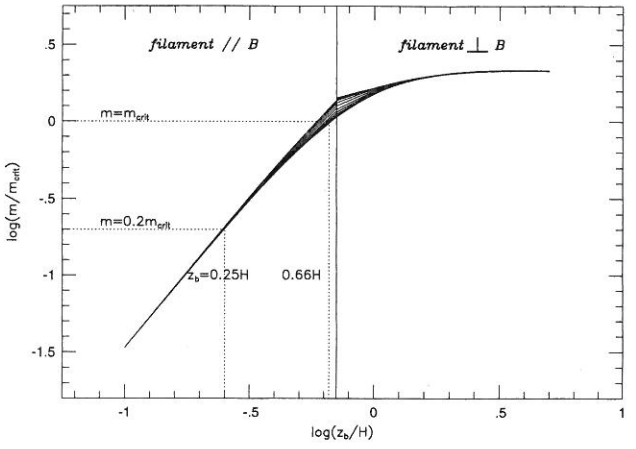

Fig. 2 The line mass (mass per unit length) of the filament expected to fragment from the layer with various half thicknesses. Each curve represents the line mass for various values of magnetic fields. These values hardly depend on the strength of magnetic fields.

Does "τ =1" Terminate the Isothermal Evolution of Collapsing Clouds ?

Hirohiko MASUNAGA, Shu-ichiro INUTSUKA
(Division of Theoretical Astrophysics · NAOJ)

We examine when gravitationally collapsing clouds terminate their isothermal evolution. According to our previous work, the condition with which isothermality is broken down is classified into three cases, i.e., when,

(1) the compressional heating rate overtakes the thermal cooling rate,
(2) the optical depth for thermal radiation reaches unity, or
(3) the compressional heating rate becomes comparable to the energy transport rate due to radiative diffusion.

In the present paper this classification is extended to more general values of the initial cloud temperature and opacity, and we determine the critical densities with which these conditions are satisfied (see Figure). For plausible values of the initial temperature and opacity, we find that the isothermal evolution ceases when Case (1) or (3) is satisfied, and Case (2) has no significance. We emphasize that the condition that "the optical depth equals unity" never terminates isothermality but non-isothermal evolutions begin either earlier or later depending on the initial temperature and opacity. This result contrasts with the conventional idea that opaqueness breaks isothermality.

On the basis of the critical density discussed above, the minimum Jeans mass for fragmentation is reconsidered. In contrast to the results by previous authors that the minimum Jeans mass is insensitive to the initial temperature and opacity, we find that the minimum Jeans mass can be substantially larger than the typical value of a few hundredths of a solar mass depending on the initial temperature and opacity. In particular, the minimum Jeans mass is inversely proportional to metallicity for low-metal clouds. Finally, our critical densities would be helpful for hydrodynamic simulations which are intended to simply handle the hardening of the equation of state.

Reference

Masunaga, H., and Inutsuka, S.: 1999, *Astrophys. J.*, **510**, 822

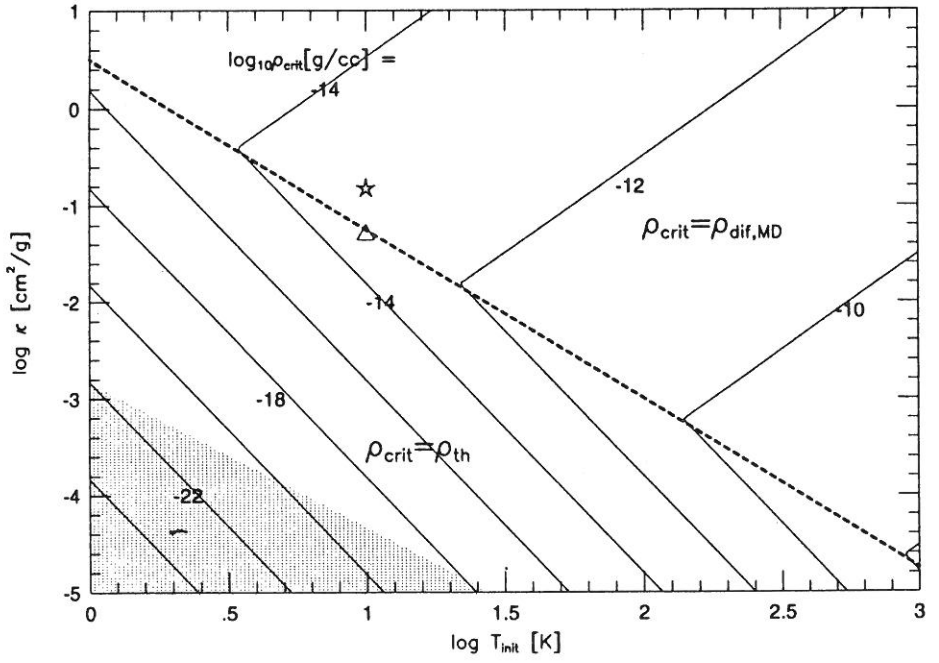

Figure

Young Brown Dwarfs in Star-forming Regions

Motohide TAMURA, Yo-ichi ITOH, Tadashi NAKAJIMA
(Devision of Optical and Infrared Astronomy · NAOJ)
Yumiko OASA
(University of Tokyo)

Recent discovery of brown dwarfs and indirect detection of extrasolar planets have made the studies on the very-low mass stars one of the hottest fields in astronomy. Although a number of brown dwarfs have been discovered so far, little is known on the formation of these very low-mass objects. Since 1990's our group has conducted extensive near-infrared surveys of star-forming regions at Kitt Peak, Cerro Toloro, Palomar, Mauna Kea, and Okayama. One of the main goals of these surveys is to make a census of young stellar objects (YSOs) in these star-forming regions. Since we are mainly interested in low-mass stars, our deep surveys are mainly concentrated in nearby star forming clouds such as the Taurus and Chamaeleon dark clouds. As a result, we have found a number of very low-luminosity (VLL) YSO candidates which have near-infrared excesses. These sources are similar to T Tauri stars (TTSs) except for their extreme faintness: they are 0.001 times fainter than the TTSs in the same region and even fainter than the very low-luminosity (VLL) YSOs that we discovered in the Taurus molecular clouds (Itoh, Tamura, & Gatley 1996). Comparisons with the theoretical evolutionary tracks for very low-mass stars, we roughly estimate the mass of these objects to be substellar (< 0.075 $M_\odot$). Some of them are estimated to be only several tens of the Jupiter mass. Therefore, we suggest that the VLL-YSOs discovered in our surveys are young brown dwarfs still embedded in molecular clouds. Some of them are found as companions and some as isolated.

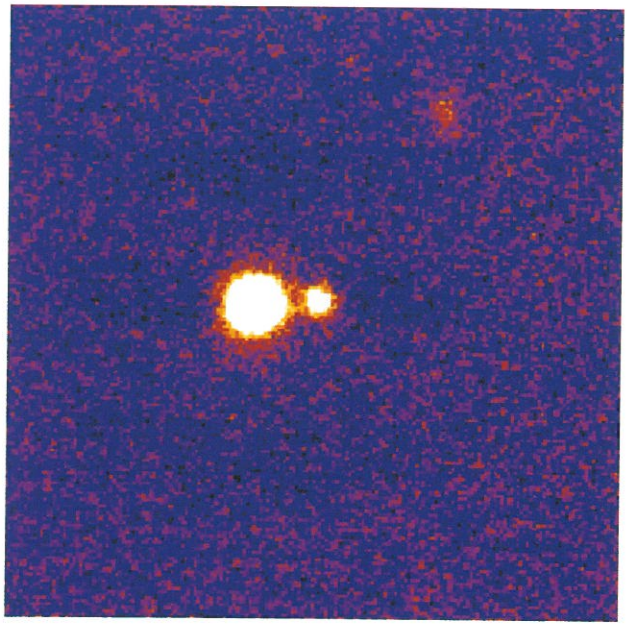

Fig. 1 2 micron image of a candidate of young brown dwart in Taurus (ITG45B; left).

Reference

Itoh, Y., Tamura, M., and Gatley, I.: 1996, *Astrophy. J.*, **465**, L129
Tamura, M. et al.: 1998, *Science*, **282**, 1095

Circular Polarization in Star-Forming Regions: Implications for Bio-molecular Homochirality

J. Bailey
(Anglo Australian Observatory)
A. Chrysostomou
(Joint Astronomy Centre)
J. H. Hough, T. M. Gledhill, A. McCall, S. Clark
(University of Hertfordshire)
F. Menard
(Observ. de Grenoble)
Motohide. Tamura
(Division of Optical and Intrared Astronomy)

Strong infrared circular polarization resulting from dust scattering in reflection nebulae in the Orion OMC-1 star-formation region has been observed. Circular polarization at shorter wavelengths might have been important in inducing chiral asymmetry in interstellar organic molecules that could be subsequently delivered to the early Earth by comets, interplanetary dust particles, or meteors. This could account for the excess of L-amino acids found in the Murchison meteorite and could explain the origin of the homochirality of biological molecules. (Quoted from *Science*, **281**, 1998)

Reference

Bailey, J. et al.: 1998, *Science*, **281**, 672

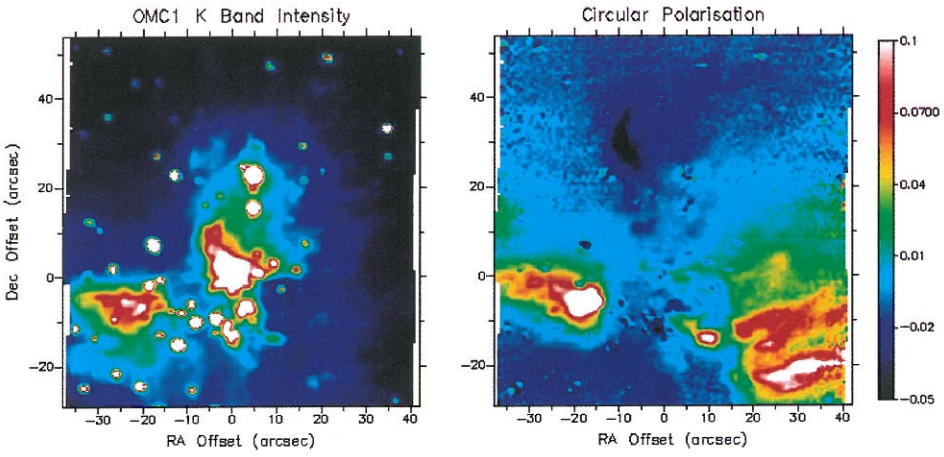

Fig. 1 2.1 micron images of surface brightness (left) and circular polarization (right) of the Orion BN/KL.

Magnetically Driven Jets from Accretion Disks III: 2.5D Nonsteady Simulations for Thick Disk Case

Takahiro KUDOH, Kazunari SHIBATA
(Division of Solar Physics · NAOJ)
Ryoji MATSUMOTO
(Chiba University)

We present the results of 2.5-dimensional MHD simulations of jet formation by magnetic accretion disks in which both ejection and accretion of disk plasma are included self-consistently. Although the jets in nonsteady MHD simulations (e.g., Uchida & Shibata 1985)have often been described as transient phenomena resulting from a particular choice of initial conditions, we found that the characteristics of the nonsteady jets are very similar to those of steady jets: (1) The ejection point of the jet, which corresponds to the slow magnetosonic point in steady MHD jet theory, is determined by the effective potential resulting from gravitational and centrifugal forces along a field line (Blandford & Payne 1982). (2) The dependences of the velocity (v_z) and mass outflow rate ($\dot{M}_w$) on the initial magnetic field strength are approximately

$$\dot{M}_w \propto B_0 \text{ and } v_Z \propto \left(\frac{\Omega_F^2 B_0^2}{\dot{M}_w}\right)^{1/3} \propto B_0^{1/3},$$

where B_0 is the initial poloidal magnetic field strength, and Ω_F is the 'angular velocity of the field line' (essentially the Keplerian angular velocity where the jet is ejected). These are consistent with the results of 1D steady solutions (Kudoh & Shibata 1997a), although their explanation is a little more complicated in the 2.5D case, due to an avalanche-like accretion flow that is present. The dependence of the accretion rate ($\dot{M}_a$) on the initial field strength is given by $\dot{M}a \propto B_0^b$ where $b \sim 1.4$ from the simulations and $b \simeq 2$ from the semi-analytical results. We also confirm that the velocity of the jet is of order of the Keplerian velocity of the disk for a wide range of parameters. We conclude that the ejection mechanism of nonsteady jets found in the 2.5-dimensional simulations can be understood using the steady state theory even when nonsteady avalanche-like accretion occurs along the surface of the disk. Nevertheless, it must be stressed that the jet and accretion never reach a steady state in our simulations, in which the back reaction of the jet on the disk is included self-consistently.

(From the abstract of the paper listed in the reference.)

References

Kudoh, T., Matsumoto, R., and Shibata, K.: 1998, *Astrophys. J.*, **508**, 186

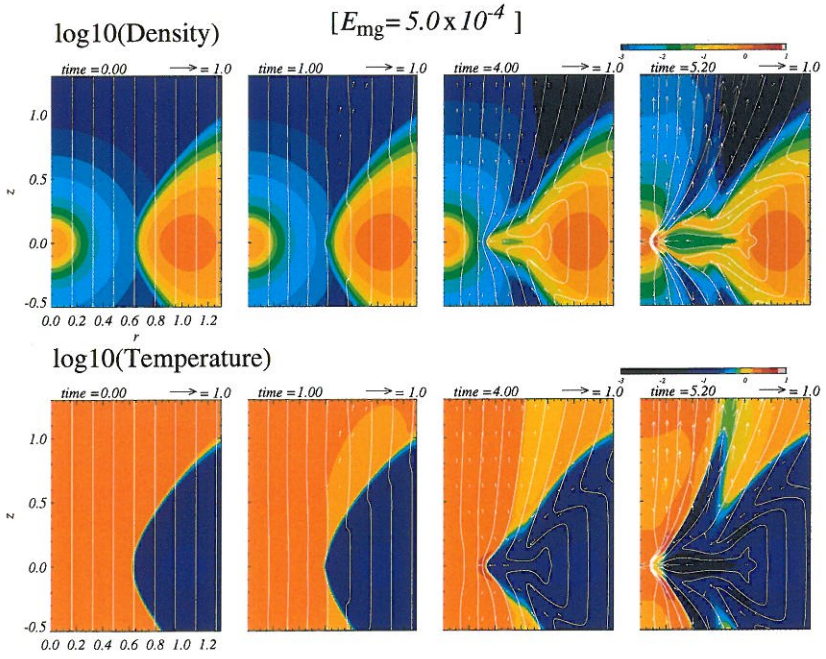

Fig.1- Time evolution of the density (upper) and the temperature (lower). Time $t \sim 2\pi \simeq 6.28$ corresponds to one Keplerian orbit at $(r,z)=(1,0)$. White vertical lines are magnetic field lines. Arrows show the poloidal velocity vectors normalized by the Keplerian velocity at $(r,z) = (1,0)$.

Alfvén Wave Model of Spicules and Coronal Heating

Takahiro KUDOH, Kazunari SHIBATA
(Division of Solar Physics · NAOJ)

Magnetohydrodynamic (MHD) simulations are performed for torsional Alfvén waves propagating along an open magnetic flux tube in the solar atmosphere. It is shown that, if the root mean square of the perturbation is greater than ~ 1 km/s in the photosphere, (1) the transition region is lifted up to more than ~ 5000 km (i.e., the spicule is produced), (2) the energy flux enough for heating the quiet corona (~ 3.0 $\times 10^5$ erg/s/cm^2) is transported into the corona, and (3) nonthermal broadening of emission lines in the corona is expected to be ~ 20 km/s. We assumed that the Alfvén waves are generated by *random motions* in the photosphere. As the Alfvé n waves propagate upward in the solar atmosphere, longitudinal motions are excited by the non-linear couplings. The longitudinal motions propagate upward as slow or fast waves and lift up the transition region (i.e., the spicule is produced). A part of the Alfvén waves are reflected in the transition region, but the remaining waves propagate upward to the corona and contribute both to the heating of the corona and the non-thermal broadening of emission lines. The result of our simulation would suggest that the quiet hot corona, nonthermal broadening of lines, and spicules are caused by Alfvén waves which are generated in the photosphere.

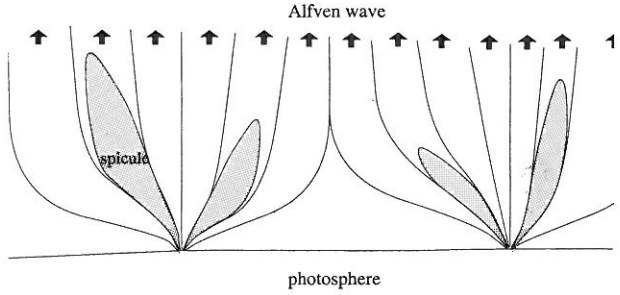

fig.1- A schematic picture of spicules and magnetic flux tubes in the solar atmosphere. The entire area of the solar atmosphere is not covered by spicules, but may be occupied by magnetic flux tubes extending from the photosphere into the corona.

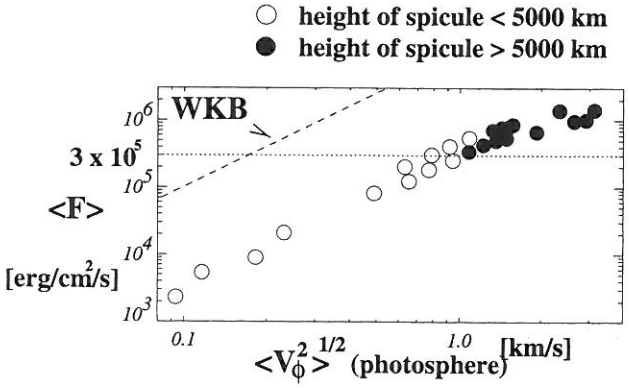

fig.2- Mean value of the energy flux in the corona as a function of $<v_\phi^2>^{1/2}$ in the photosphere. A dashed line shows the result of WKB approximation.

Reference

Kudoh, T., and Shibata, K.: 1998, *Astrophys. J.*, **514**, 493

* Kyoto University

Thickness Variation of Coronal X-ray Loops of the Sun

Huaning WANG, Takashi SAKURAI
(Division of Solar Physics · NAOJ)

Coronal loops observed with the soft X-ray telescope on board Yohkoh often show that their cross-section is nearly constant along their length. If the coronal loops align along the magnetic field lines and the field in the corona is approximately a vacuum field (namely, electric currents in the corona are negligible), the loops should expand more toward their apex. One explanation proposed so far is that the electric currents flowing in the loops constrict their volume and create magnetic tubes with nearly constant cross section.

Although this 'pinch effect' should certainly work in a volume surrounded with a fixed wall, in an open space like the solar corona, the tubes with electric currents may expand and fill a larger volume instead of pinching themselves.

We studied the changes in the cross section of magnetic flux tubes as the electric currents are increased, by using a simple analytic solution of an equilibrium field. We found that the magnetic tubes with nearly constant cross section appear only at some specific locations in the field geometry. The 'specific locations' appear at the magnetic polarity inversion line and when the fields are highly sheared.

References

Wang H., and Sakurai, T.: 1998, *Publ. Astron. Soc. Japan,* **50**, 111-123,
Sakurai, T., and Wang, H.: 1998, *Proc. SOLTIP,*

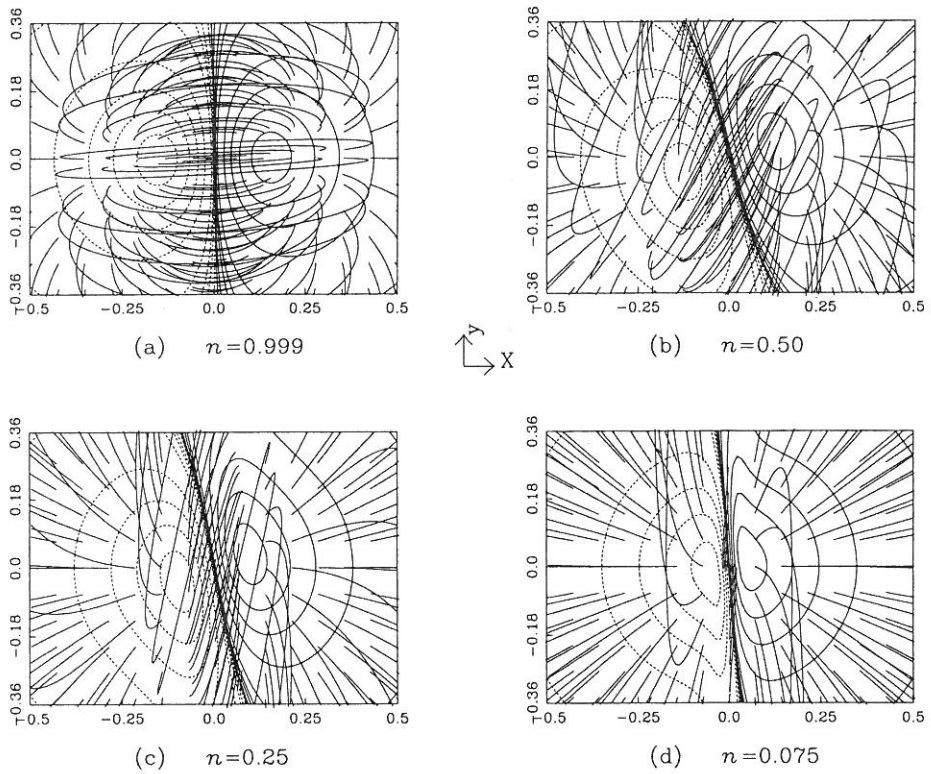

Changes of field line configuration as the electric currents are increased. Here n=0.999 corresponds to a configuration with nearly a current-free state, whereas n=0.0075 corresponds to a configuration with a large amount of electric currents.

Evolution of Eruptive Flares
II. The Occurrence of Locally Enhanced Resistivity

Tetsuya MAGARA
(Kyoto University)
Kazunari SHIBATA
(Division of Solar Physics · NAOJ)

In this paper we study resistive processes in the preflare phase of eruptive flares by means of the 2.5-dimensional MHD numerical simulation. According to many detailed observations of solar flares, their evolution is characterized by several phases, each of which has a distinct nature. In the first phase, some kinds of radiation begin to be enhanced gradually, which implies the occurrence of the preflare heating. Then, at a certain time, that gradual energy-release phase is replaced by the violent energy-release phase in which a huge amount of energy is released in various forms. So far, the nature of this violent energy-release phase has been well studied by using a flare model based on the fast magnetic reconnection , though those problems of the preflare heating and the transition from the gradual energy-release phase to the violent one have not been sufficiently discussed yet. In this paper, in order to tackle these problems, we start with a 2.5-dimensional force-free current sheet under a uniformly distributed resistivity, which is subject to a very small random velocity perturbation. At first the evolution enters on the linear stage of tearing instability and later a sufficient amount of thermal energy is produced in the nonlinear stage, which is considered to have a relation with the preflare heating. In this nonlinear stage, the component of magnetic fields perpendicular to the sheet (perpendicular magnetic fields) flows away from X-points formed in the sheet and eventually the current-sheet collapse occurs at these points (see Fig. 1). That collapse makes the thickness of the sheet reduced strongly if the magnetic Reynolds number is quite large and the plasma beta is quite low. Since the formation of thin current sheet leads to the occurrence of locally enhanced resistivity (anomalous resistivity), the transition from the gradual energy-release phase under a uniformly distributed resistivity to the violent one under a locally enhanced anomalous resistivity can be accomplished, which causes the fast magnetic reconnection responsible for various explosive phenomena in the sun.This abstract is cited from Magara & Shibata (1999).

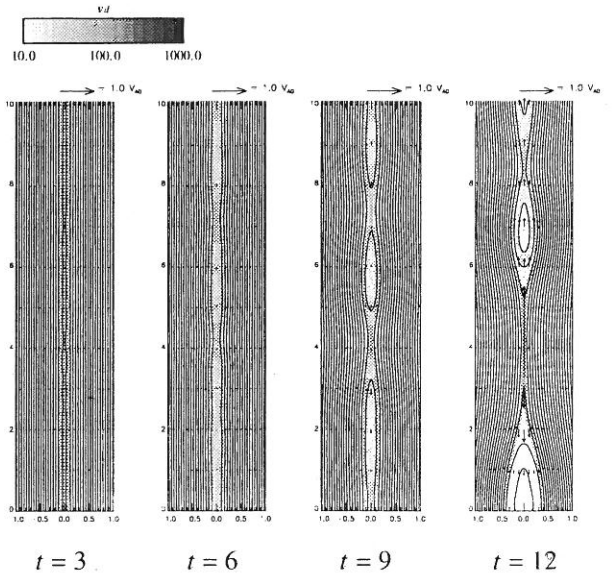

Fig. 1 Evolution of the typical case. Contour lines, arrows, and a grayscale map represent the magnetic field lines, velocity field, and the value of drift velocity ($v_d \equiv |j| / \rho$) projected onto the plane.

Reference

Magara, T., and Shibata, K.; 1999, *Astrophys. J.*, **514**, 456

X-ray Plasma Ejection Associated with an Impulsive Flare

Masamitsu OHYAMA*, Kazunari SHIBATA*
(Division of Sloar Physics · NAOJ)

The 1992 October 5 flare was associated with an X-ray plasma ejection. Although the ejected plasma looks like a blob (or plasmoid) in short exposure images (Fig. 1), in long exposure images it appears to be penetrated by or connected to the top of a large scale loop. The ejecta had started to rise with the speed of $\sim$ 250 km s^{-1} before the main peak of the hard X-ray emission and was accelerated during the impulsive phase (to $\sim$ 500 km s^{-1}). We derived the physical parameters of the ejected plasma and obtained the following results: (1) The temperature of the ejected plasma was 10.6 ± 3.6 MK. (2) Its density was $(8 - 16) \times 10^9$ cm^{-3} and was an order of magnitude larger than that of the typical active-region corona. (3) The mass of the ejected plasma was $(2 - 4) \times 10^{13}$ g. (4) The kinetic energy of the ejecta was smaller than the thermal energy content of the flare loop. The overall features and evolution of the hot plasma ejection and flare are in rough agreement with those expected from the reconnection model (Fig. 2), and the reconnection rate ($M_A = V_{in}/V_A$) is estimated to be $\sim$ 0.02, where V_{in} is the speed of the inflow into the reconnection region, and V_A is the Alfvén speed. Result (4), however, is not consistent with the assumption in some reconnection models that an ejected plasma stretches the overlying magnetic fields to form a current sheet and hence leads to magnetic reconnection. Instead, our results suggest that both X-ray plasma ejection and reconnection are a consequence of a common dynamical process such as the global MHD instability.

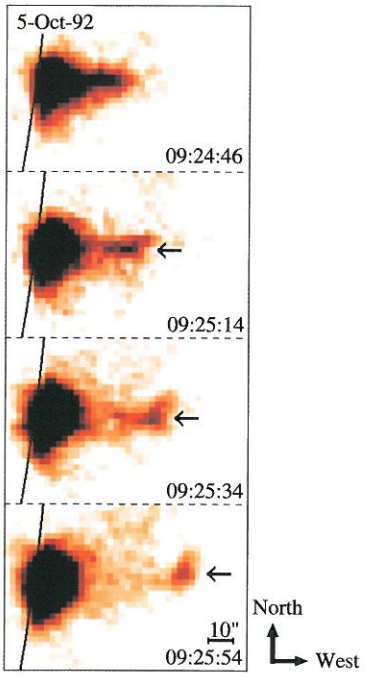

Fig. 1. Sequence of Soft X-ray images of the flare on 1992 October 5. The ejected plasma is indicated by the arrows. The curves indicate the solar limb; 1 arcsec is $\sim$ 726 km.

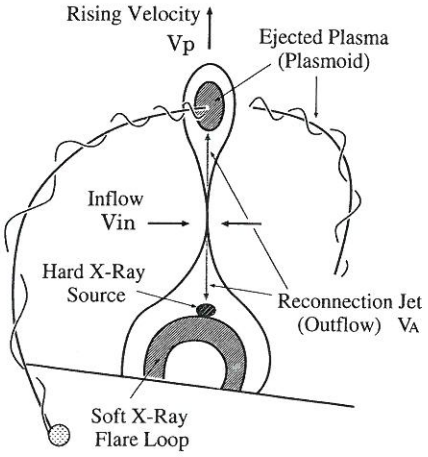

Fig. 2. Three-dimensional view of the plasma ejection.

Reference

Masuda, S., Kosugi, T., Hara, H., Tsuneta, S., and Ogawara. Y.: 1994, *Nature.*, **371**, 195-197.

Ohyama, M., and Shibata, K.: 1997, *Publ. Astron. Soc. Japan.*, **49**, 249-261.

Ohyama, M., and Shibata, K.: 1998, *Astrophys. J.*, **499**, 934-944.

Shibata, K., Masuda, S., Shimojo, M., Hara, H., Yokoyama, T., Tsuneta, S., Kosugi, T., and Ogawara, Y.: 1995, *Astrophys. J. Left.*, **451**, 83-85.

* Kyoto University

Heating of Erupting Prominences Observed at 17 GHz

Yoichiro HANAOKA
(Solar Radio Observing Facilities of Nobeyama Radio Observatory, NAOJ)
Takehiko SHINKAWA
(Communications Research Laboratory)

We found evidence that heating of erupting prominences occurs at the beginning of two events on 1992 November 5 (McAllister et al. 1996) and on 1994 February 20 (Shinkawa et al. 1999), which were observed with the Nobeyama Radioheliograph at 17 GHz. Both of the events are eruptions of the prominences on the disk, which are seen as the eruptions of dark filaments. The radio images of the events show very similar changes as follows. Shortly after the filaments began to be accelerated rapidly and to detach from the disk, the filaments apparently disappear. However, when the moving filaments pass above bright plage regions, the plage regions become dark. These facts indicate that the brightness temperature of the dark filaments increase to the temperature of the quiet disk at the beginning of the abrupt eruptions, while the filaments keep their large optical thickness. After the rapid increase, the brightness temperature does not change significantly during the motion of the filaments. In contrast to H-alpha, the visibility of prominences in 17 GHz images are not affected by Doppler shifts. Therefore, changes of the brightness temperature reflect changes of the physical parameters of prominences. Heating of the surface of the cool core of the prominences up to the transition region temperature is most plausible to explain the observed increase of the brightness temperature at 17 GHz.

[This is the abstract of a paper by Hanaoka, Y. and Shinkawa, T. (1999, Astrophs. J., **510**, 466).]

References

McAllister, A.H., Kurokawa, H., Shibata, K., and Nitta, N.: 1996, *Solar Physics*, **169**, 123.
Shinkawa, T. et al.: 1999, in preparation.

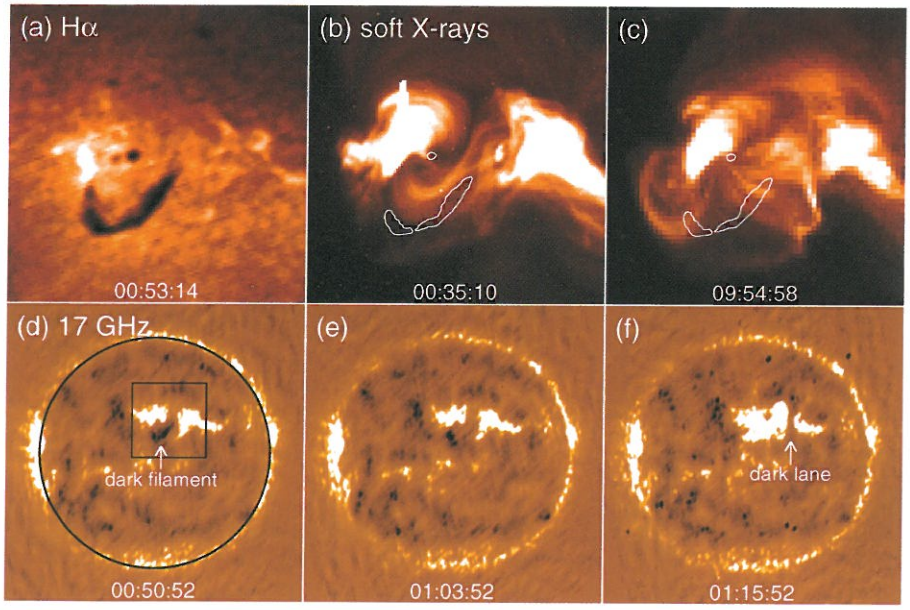

Fig. 1 (a) An H-alpha image taken with the Flare-Monitoring Telescope at Hida Observatory before the eruption. (b) (c) Soft X-ray images taken with the SXT on board Yohkoh. The dark filament seen in the H-alpha picture is shown with contours. Before the eruption (b), X-ray loops are nearly parallel to the filament due to strong shear, but after the eruption (c), they become roughly perpendicular. (d — f) Images at 17 GHz taken with the Nobeyama Radioheliograph. The whole Sun is shown, and the position of the solar limb and the field of view of (a—c) are shown in (d). The filament in (d) mostly disappears in (e), but it can be seen in (f) as a dark lane above a plage region again.

Radio Detection of Umbral Oscillations

G. B. GELFREIKH
(Pulkovo Astronomical Observatory, Russia)
V. GRECHNEV
(Sib IZMIR, Russia)
Takeo KOSUGI, Kiyoto SHIBASAKI
(Division of Radio Astronomy · NAOJ)

Using microwave observations made with the Nobeyama Radioheliograph ($\lambda = 1.76$ cm), we have studied temporal variations of sunspot-associated sources in the circularly polarized component. For all three cases of well-developed and rather stable sunspots we found nearly harmonic oscillations with periods in a range of 120 — 220 s. In one case of an unstable and quickly evolving active region, the fluctuations appear to be irregular with no dominant period. Sunspot-associated solar radio sources are known to be generated by cyclotron radiation of thermal electrons in magnetic tubes of sunspots at the level of the lower solar corona or chromosphere-corona transition region (CCTR). At the wavelengths of 1.76 cm, the polarized emission arises in a layer where the magnetic field is B = 2000 G (assuming the emission generated at the third harmonic of electron gyrofrequency).

We suggest that the observed effect is a manifestation of the well-known 3-min oscillations observed in the chromosphere and photosphere above sunspots. The observed effects are believed to be a result of resonance oscillation of MHD waves inside a magnetic tube, Radio observations of this phenomenon open a new tool for studying regions of reflection of MHD waves near CCTR level. The method is very sensitive both to the height of the CCTR and magnetic fields above sunspots. Thus, detection of oscillations of the height of the transition region even with an amplitude of a few km RATAN-600 allows us to conclude that oscillations in magnetic field (Gelfreikh, G.B., Grechnev, V., Kosugi, T., and Shibasaki, K., 1999, *Solar Phys.*, **185**, 177 — 191.) strength of about 4 G could be responsible for the effect are reliably registerd. The appearance of the famous 5 -min oscillations in the solar atmosphere was also registered in some spectra of radio oscillations.

(Quoted from *Solar Phys*, **185**, (1999))

Reference

Gelfreikh, G.B., Grechnev, V., Kosugi, T., and Shibasaki, K.,: 1999, *Solar Phys.*, **185**, 177 — 191.

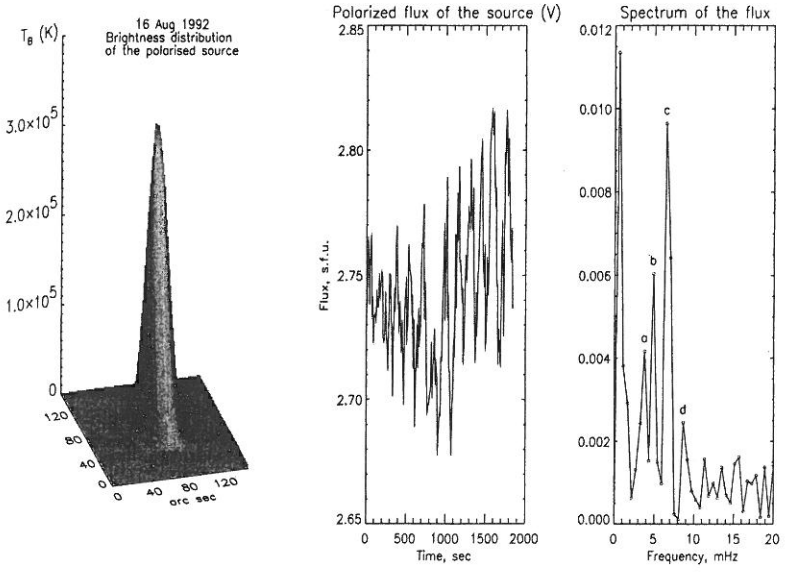

Fig. Spatial structure of the polarized component of the AR7260 (16 Aug., 1992) (left), temporal variation of the source flux (center), and the harmonic analysis of the temporal variation (right). The periods of the peaks a - d correspond to 265, 205, 154 and 115 sec. respectively.

Microwave Blobs above the Tops of Preflare Loops in the Solar Corona

Kuniko HORI, Kiyoto SHIBASAKI
(Division of Radio Astronomy·NAOJ)
Ken-ichi FUJIKI (Nagoya University)
Hideki KOSHIISHI (NASDA)

Solar flare is an eruptive energy release and dissipative process. So far, observational study of *the preflare phase*, in which energy build-up and weak dissipation process takes place prior to a flare, is still insufficient. We observed weak preflare activities seen in microwaves (17 GHz) with Nobeyama Radioheliograph (hereafter NoRH). The NoRH is a solar dedicated radio interferometer, monitoring the whole Sun at 17 & 34 GHz each day, continuously with temporal resolution of 1 s. At 17 GHz, NoRH has a dynamic range up to 25 dB and spatial resolution of 10 — 20 arcsec, which enables us to analyze weak sources in the preflare phase. In this paper we present our new findings ; the formation of a faint filamentary structure (or an arch) above the tops of preflare loops in microwaves (see Hori 1999 ; Hori *et al.* 1999).

We analyzed two preflare events in which an arcade of loops located at or near the solar limb. Both of the events show the following characteristic features in common (Fig. 1; contours): The initial activation starts in a pre-existing mound-shaped source, which corresponds to the end of an soft X-ray arcade loops (see *Yohkoh* SXT image; color). The brightness temperature (T_b) increases at the base of the mound,as indicated by an arrow in panel a. The mound is initially surrounded by a faint extended source (T_b = a few $\times$ 10^4K). Above the activated mound, a compact blob appears in the faint source (an arrow in panels *b* and *c*). The blob expands horizontally toward different directions and forms filamentary structures (or arches),which basically agree with directions of ridges seen in the pre-existing weak source (see arrows in the bottom panel). One of the motions runs along the ridge of the soft X-ray arcade,as indicated by dotted arrows in panels *c* and *d*. Before the flare start time, which is suggested by the abrupt appearance of a circularly polarized source at the base of the mound (*d*; a brown contour), *thermal free-free emission* is the most relevant emission mechanism for these activities.In this case, the apparent motion of radio sources can be interpreted as field-aligned mass motion.

According to temperature maps obtained with SXT images, the highest-temperature region (a few MK) located *between* the mound and the overlying blob. We discuss the possibility of *magnetic reconnection* progressing the middle place during the preflare phase.

Reference

Hori, K.: 1999, *Adv. Space Res.*,, in press
Hori, K., Fujiki, K., and Koshiishi, H.: 1999, *Astrophys. J.*, submitted.

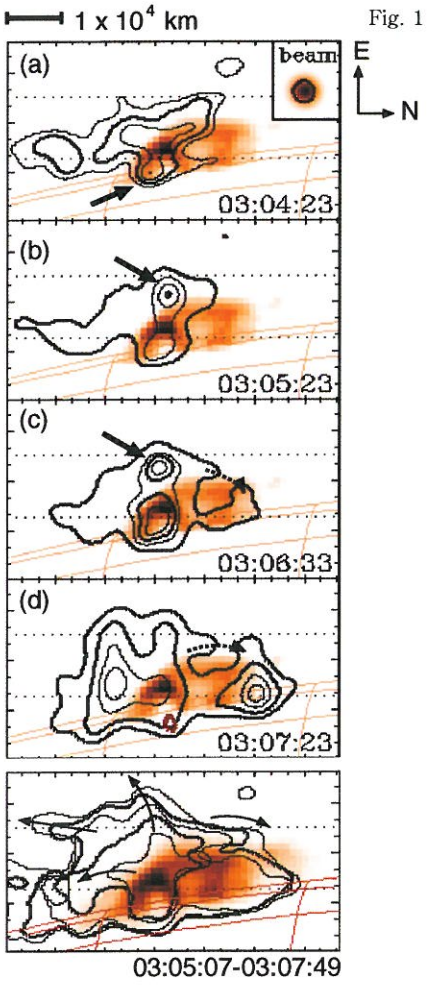

Fig. 1 Evolution of the 1993 June 25 flare. A series of NoRH 17-GHz maps (contours) overlaid on a soft X-ray snapshot taken at 03 : 14 : 09 UT with *Yohkoh* SXT (colorscale). Upper panel : Thick and thin contours are for T_b = [2, 5] $\times$ 10^4K and 30-, 60-, and 90-% levels of the peak intensity, respectively, for the Stokes-I component. The brown contour in panel *d* show T_b = 1 $\times$ 10^4K for the Stokes-V component.Bottom panel: Motions seen in the microwave source. The contour levels are, from inside to outside, T_b = [2.2, 2.2, 2.0, 1.5, 1.0] $\times$ 10^4K taken at several times from 03 : 05 : 07 to 03 : 07 : 49 UT. The heliographic grid is shown with a spacing of 5 degrees in orange lines.The 17-GHz beam size (HPBW) is shown at the top right corner. Solar east is up, and north is to the right.

Asteroid Lightcurve Observations near Stationary Points: (4179) Toutatis in 1997 February

Tsuko NAKAMURA
(Division of Optical and Infrared Astronomy · NAOJ)
Tetsuharu FUSE
(Grad. Univ. for Advanced Studies)

Lightcurve observations of asteroids with long-spin periods (say, more than a few days) are particularly important regarding the detection of a non-principal axis spin state. However, it is not easy for such observations to achieve photometric accuracy comparable to that for short-period spin asteroids, since slow-spin asteroids inevitably require long duration and coordinated observations and the use of different reference stars during a run. We propose here the advantage of observations near stationary points for long-spin asteroids, where the same reference stars can be used throughout.This proposal was tested for CCD lightcurve observations of asteroid (4179) Toutatis, which were performed near its stationary point in 1997 February. From six night observations spanning 11 days, a spin period of 7.50 ± 0.2 d was obtained using two independent methods of period analysis; this value has been found to be in fairly good agreement with the periods obtained by Hudson and Ostro(1995, AAA 64.098.037), and Spencer et al.(1995, AAA 64.098.052).

Key words: Asteroids: individual (Toutatis) —— Photometry —— Rotation

(Quoted from *Publ. Astron. Soc. Japan,* **50**, (1998))

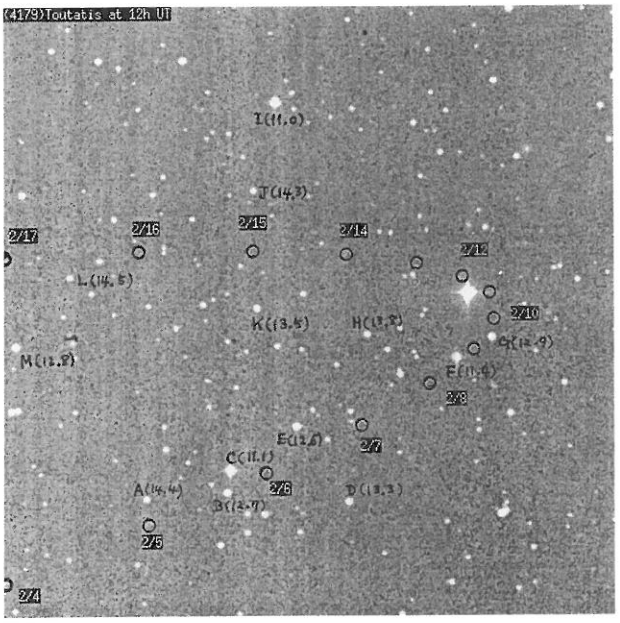

Apparent motion of Toutatis near its stationary point in 1997 February. The 12^h UT positions are indicated by open circles. The field of view is 15′×15′, with the north up and the east left. The photometric reference stars adopted in our observations are indicated by an alphabetical letter with *V*-mag in parrentheses. The magnitudes were taken from the Guide Star Catalog prepared for the Hubble Space Telescope (Russell et al. 1990).

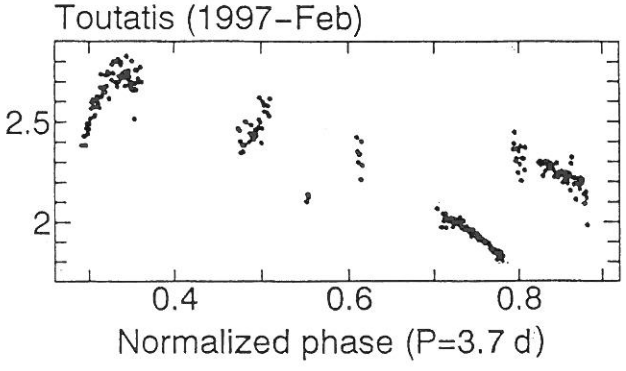

Synthesized lightcurve of Toutatis normalized to the rotational phase with P_T=7.5d. The complicated behavior seems to suggest a yumbling rotation of this asteroid.

Reference

Spencer, J.R., Nakamura, T. et al.: 1995, *Icarus,* **117**, 71-89.
Nakamura, T., and Fuse, T. : 1998, *Publ. Astron. Soc. Japan,* **50**, 531-536.

A Simulation Study of Lunar Gravity Field Estimation

Kohji MATSUMOTO, Kohsuke HEKI
(Division of Earth Rotation · NAOJ)
D. D. ROWLANDS
(NASA/ Goddard Space Flight Center)
R. FLOBERGHAGEN
(Delft Institute for Earth-Oriented Space Research)

We will research in detail the lunar gravity field in SELENE (SELenological and ENgineering Explorer), to be launched in 2003, by various tracking of a lunar orbiter. Lunar gravity harmonic coefficients have been conventionally determined by 2-way Doppler tracking of lunar orbiters. This way of tracking, however, can not directly observe the lunar far-side gravity field because the period of revolution of the Moon is equal to that of rotation. In order to overcome this present situation, we propose in the SELENE project 4-way Doppler tracking by means of relay sub-satellite which relays Doppler signal to/from the lunar orbiter. The 4-way Doppler tracking will, for the first time in the world, directly observe the lunar far-side gravity field. SELENE gravimetry is also characterized by differential VLBI(ΔVLBI) between VLBI radio source on board the lunar orbiter and background quasar, which measures position and velocity of the lunar orbiter in a plane perpendicular to Earth-Moon direction to which 2-way Doppler measurements are sensitive. Numerical simulation study is done by GEODYN II/SOLVE softwares in collaboration with NASA/Goddard Space Flight Center in order to check the planned measurement scenario.

Shown in Fig. 1 and 2 are anticipated selenoid height error with 2-way Doppler data only and with far-side 4-way Doppler data included, respectively. Fig. 2 suggests that 4-way Doppler measurements significantly improve far-side selenoid to the accuracy comparable to near-side selenoid. Fig. 3 compares orbit determination accuracy of the lunar orbiter between the case of 2-way Doppler data only and the case of both ΔVLBI and 2-way Doppler data used, respectively. Δ VLBI contribution is significant when determining short arc orbit, because 2-way Doppler data and ΔVLBI data provide three-dimensional position and velocity information of the lunar orbiter. This property is very important for determining lunar gravity field from tracking data of SELENE lunar orbiter of which orbit will be perturbed by attitude control maneuvers every several revolutions.

This study shows that new measurement methods proposed in the SELENE project will result in a high-precision lunar gravity filed model, which will help us address selenophysical issues, such as the origin of lunar dichotomy, lunar thermal history, lunar isostasy, and the lunar moment of inertia (i.e., the existence of the metallic core).

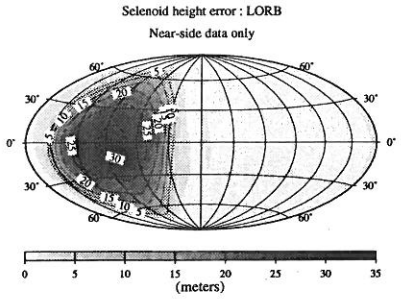

Fig. 1 Anticipated selenoid height error with conventional 2-way Doppler only.

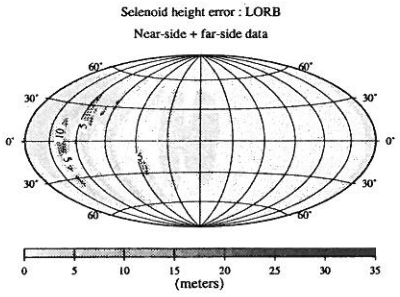

Fig. 2 Same as Fig. 1, but with far-side 4-way Doppler data included.

References

Matsumoto, K., Heki, K., and Rowlands, D.D.: 1999, *Adv. Space Res.*, in press

Heki, K., Matsumoto, K., and Floberghagen, R.: 1999, *Adv. Space Res.*, in press

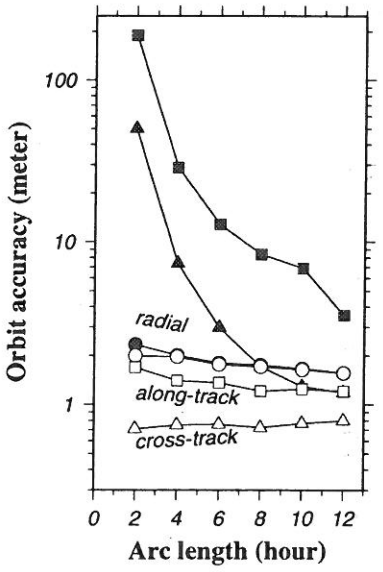

Fig. 3 Comparison of the short-arc orbit determination accuracy; solid symbols, values when only 2-way Doppler used; open symbols, values when Δ VLBI data are added.

HD TV Observation of the Strong Activity of Giacobinid Meteor Shower in 1998

Jun-ichi WATANABE
(Public Relations Center · NAOJ)
Shinsuke ABE
(Graduate University of Advanced Studies)
Masaaki TAKANASHI, Takema HASHIMOTO, Oumi IIYAMA
(Nippon Meteor Soc.)
Yukihiro ISHIBASHI, Kazumasa MORISHIGE, Sozo YOKOGAWA
(University of Tokyo)

A prominent activity of the 1998 Giacobinid meteor shower was observed on October 8 in Japan. The visual hourly rate was reported as more than 100 around the peak.

We carried out a High-sensitivity HD-TV observation of this activity at the Dodaira station. The camera was composed of a large diameter image intensifier along with a 1-inch 2M-pixel FIT CCD, which gives high resolution of 1150 TV lines, so called High-Definition TV. A 35-mm camera lens of Canon EOS 50 mm (F/1.0) was used as the objective lens. This system gives a wide field of view of 32°. 7 18°. 3, along with the limiting magnitude of 8 under the conditions of the full moon.

We set up the replay of the recorded video tape at the NHK studio because we need a digital video tape recorder of D5 type, which is specially designed for the HD TV format. Although our observation was carried out from 11h 02m UT through 19h 00 m UT, we selected the data taken until 15h UT for this analysis, because the Giacobinids was hardly noticed after this time.

We inspected the video tape replayed, and picked up all the meteors, and recorded the time of the apparition of each meteor along with the rough estimate of the maximum brightness compared to the field stars.

We detected 341 Giacobinid meteors along with 127 sporadic meteors, and derived time variation of the activity as shown in the figure.

The peak of the activity was around 13h 05m UT, which corresponded to the solar longitude 195°. 071 (equinox J2000.0). This is different from the expected maximum of the Giacobinids at the solar longitude 195°. 4 (equinox J2000.0). The peak influx rate of the meteoroids of $1.6 \times 10^{-5} km^{-2} s^{-1}$, which is thought to be comparable to that observed in 1985.

Reference

Watanabe, J., Abe, S., Takanashi, M., Hashimoto, T., Iiyama, O., Ishibashi, Y., Morishige, K., and Yokogawa, S.: 1999., *Geophys. Res. Lett.* **26-8**, 1117-1120.

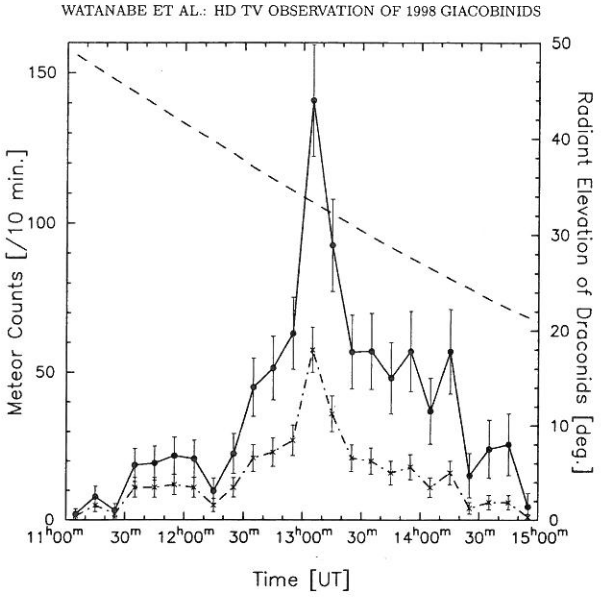

Figure. Time variation of the number of Giacobinids observed in HD TV camera system at ten minitues interval. Broken line is the row number, and the solid line is the number after the correction of the radiant point elevation, which is also shown in solid curve.

Isophote Maps of the Gegenschein Obtained by CCD Observations

Masa-aki ISHIGURO, Ryosuke NAKAMURA, Tadashi MUKAI, Tsuyoshi WATANABE
(Kobe University)
Hideo FUKUSHIMA, Jun-ich WATANABE (Public Relations Center · NAOJ)
Daisuke KINOSHITA (Science Univ. of Tokyo)
J. F. James (Univ. of Manchester)

1. Introduction

The Gegenschein is an extremely faint light around the antisolar point. There was some hypothesis on the origin; reflection of sunlight by particles concentrated near the libration point in the sun-earth-particle system, emission by the earth's gaseous tail, scattering by earth's dust tail cloud, and so on. Since the Gegenschein is still present out to 1.86 AU in the Pioneer 10 data (Weinberg *et al.*, 1973), it turned out to be the sunlight caused by back-scattering enhancement of the zodiacal dust cloud. However there remains some questions about the Gegenschein, such as the position of the maximum brightness, the exact shape and their time variation. We tried to observe the Gegenschein by using a CCD camera with wide angle/fish-eye lens.

2. Observations and Data Reduction

The photometric data presented here consist of three observations; one at Norikura (altitude 2876 m) and two Kiso 1130 m.

We observed the Gegenschein at the Norikura observatory (NAOJ) on the 18th of September. The instrument consisted of the 20 mm F5.6 wide angle lens attached to a Mutoh CV-16 CCD camera. We used the filter of Hoya G-533. At Kiso Observatory (Univ. of Tokyo, Japan) we observed from the 9th to 14th February and from 4th to the 5th March in 1997. We used a 8 mm Nikon fish-eye lens instead of 20 mm wide angle lens, the same one as we used at Norikura. Due to the comtaminations of city light from Nagoya and reflected light by the snow, data coverages are limited for $167^\circ < \lambda - \lambda_\odot < 193^\circ$, $-7^\circ < \beta < 7^\circ$ at 18th September, and $165^\circ < \lambda - \lambda_\odot < 195^\circ$, $-10^\circ < \beta < 15^\circ$ at 5th March.

In the ground observations, the observed intensity (I_{obs}) of the sky is expressed by the following equation;

$$I_{obs} = (I_{ST} + I_{ZL} + I_{AG}) \cdot e^{-\tau} + I_{SL} + I_{CL},$$

where I_{ST}, I_{ZL}, I_{AG}, I_{SL} and I_{CL} mean the the intensity of integrated starlight, zodiacal light, airglow, scattering light by lower atmosphere and the city light, respectively. τ denotes the optical depth of the atmosphere. We estimated τ from the photometry of background standard stars. Especially main contamination in visible is from OI airglow emission (557.7nm), is estimated by the function of the zenith distance and removed from the data.

3. Results

It is clear that the shape of the Gegenschein changes with the season (see Fig. 1). In addition, a center position of the maximum brightness of the Gegenschein deviates to the south in September ($-0.^\circ 4$) and to the north in March ($+0.^\circ 7$) (see e.g.Misconi, 1981). The north-south deviation found in the observations can be explained by the zodiacal cloud model having a symmetric plain deviated toward the south in September and toward the north in March. The invariant plane of the solar system is one plausible candidate.

References

Weinberg, *et al.*: 1973, *Space Research*, **XIII**, 1187
Misconi, N.Y.; 1981, *Icarus*, **47**, 265

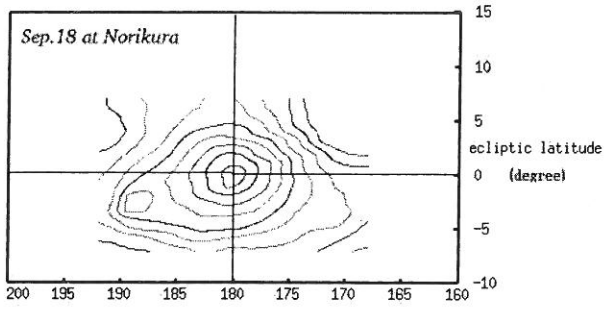

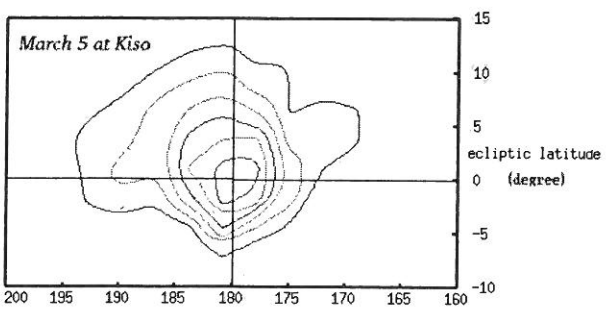

Fast Procedures Solving Kepler's Equations II: Hyperbolic and near-Parabolic Orbits

Toshio FUKUSHIMA
(Public Relations Center · NAOJ)

As we reported in the Annual Report for the year 1996, we developed a fast procedure solving the Kepler's equation for the elliptic orbits, which is frequently used in computing the Keplerian orbits as well as some numerical integrators. It runs 2.5 times or more faster than any existing procedure. As a natural extension, we developed similar fast procedures for the hyperbolic and nearly- parabolic cases (Fukushima, 1997a, 1997b, 1998). In the hyperbolic case (e>1), the standard form of Kepler's equation becomes

$$e \sinh F - F = M$$

and the extended form is expressed as

$$e\_X \sinh D + e\_Y (\cosh D - 1) - D = L$$

where F is the (hyperbolic) eccentric anomaly, M is the (hyperbolic) mean anomaly, e is the eccentricity, $L = M - F\_0$, $D = F - F\_0$, $e\_X = e \cosh F\_0$, $e\_Y = e \sinh F\_0$, L = D- and F_0 is an unknown constant. Since the both forms are nonlinear, we must solve them numerically by iteration. This time, the interval of solution is semi-infinite. Therefore, we can not apply naively the bisection method using pre-computed tables of special functions, which works in the elliptic case. In the standard form, however, the hyperbolic functions grow exponentially. Thus, we may treat the effect of linear term as a perturbation to the asymptotic solution when F is sufficiently large, say greater than 5.3 or so. After excluding this case and the case of small solution where M is so small that the solution is expressed by an inverted series, we may follow our approach succeeded in the elliptic case; the combination of the bisection method and the Newton method using the Taylor-series evaluation of special functions. The situation is almost the same in the case of extended form. As a result, the new procedures run 2.5 — 3.7 times faster than the existing procedures (Fig. 1, Fukushima 1997a, 1997b).

On the other hand, in the case when the orbit is parabola (e=1) or sufficiently close to it (for example, $0.95 < e < 1.05$), it is unappropriate to solve the elliptic or hyperbolic forms of the Kepler's equation. Gauss introduced a quasicubic form

$$w + w^3/3 = W(w)$$

as a proper form of Kepler's equation for such nealy-parabolic case. He developed a tactful method to solve this fast by using the exact solution of Barker's equation, which is a cubic equation being exact for the purely parabolic case. This Gauss' form is the first Kepler's equation being 'universal', namely covering the elliptic, parabolic, and hyperbolic cases uniformly.

It has been known as the most useful form for nearly parabolic case. Now, we developed a new procedure to solve this Gauss' form by using the fast solving procedure of Barker's equation and other techniques we have used so far. As a result, it runs 3—4 times faster than Gaussimplementation (Fig. 2, Fukushima1998).

References

Fukushima, T.: 1997a, *Cele. Mech. Dyn. Astr.*, **68**, 121.
Fukushima, T.: 1997b, *Astron. J.*, **113**, 1920.
Fukushima, T.: 1998, *Cele. Mech. Dyn. Astr.*, **70**, 115.

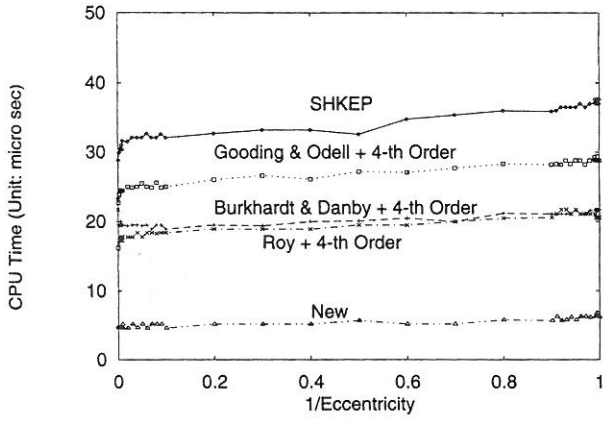

図 1

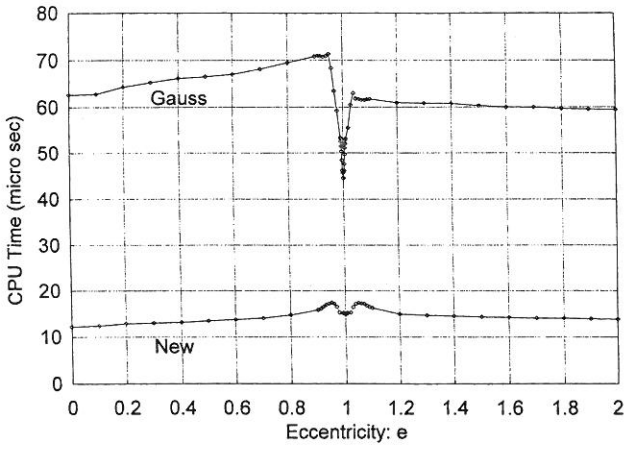

図 2

Necessary Condition for Integrability of Hamiltonian Systems Based on Differential Galois Theory

Haruo YOSHIDA
(Division of Astrometry and Celestial Mechanics · NAOJ)

On of the fundamental problem in mechanics is to decide the integrability of a given Hamiltonian system, such as the gravitational three body problem. Although the complete criterion is not yet known until know, a big progress has been made in this direction.

A Hamiltonian system with a homogeneous potential $V(q_1, q_2)$ of degree k,

$$H = \frac{1}{2}(p_1^2 + p_2^2) + V(q_1, q_2) \qquad (1)$$

has always a straight line solution, which can be written as $q_1 = 0$ by a proper rotation of coordinates. The variational equation around this straight line solution is transformed, by the change of independent variable $z = [q_2(t)]^k$, to the Gauss hypergeometric equation,

$$z(1-z)\frac{d^2\xi}{dz^2} + [c - (a + b + 1)z]\frac{d\xi}{dz} - ab\xi = 0$$

Suppose now that the system (1) is integrable, and assume that there exists an additional first integral $\Phi(q, p) = \text{const.}$, which is analytic at least in the neighborhood of the straight line solution $q_1 = p_1 = 0$. This first integral induces a first integral for the variational equation, and also a first integral for the Gauss hypergeometric equation, which is a first order ordinary differential equation. The solution of this first order ordinary differential equation is obtained in the form, $\xi = \exp[\int \zeta(z)dz]$, where $\zeta(z)$ is a solution of an algebraic equation with coefficients which are polynomials of z. This means that the solution of the Gauss hypergeometric equation is obtained only by elementary operations, that is, algebraic function, quadrature, and exponential function.

On the other hand, in 1969, T. Kimura obtained a necessary and sufficient condition for the Gauss hypergeometric equation to be solved elementally based on differential Galois theory. Let λ, μ, ν be the difference of exponents at regular singular points, $z = 0, 1, \infty$, i.e.,

$$\lambda = 1 - c,\ \mu = c - a - b,\ \nu = a - b$$

Then a necessary and sufficient condition for the Gauss hypergeometric equation to be solved elementally only by algebraic function, quadrature, and exponential function, starting from rational functions (solvable in the sense of differential Galois theory) is that

- at least one of $\lambda \pm \mu \pm \nu$ is an odd integer, or
- $\pm\lambda, \pm\mu, \pm\nu$ take values of the table of Schwarz-Hukuhara-Ohasi in an arbitrary order.

Based on this Kimura's theorem, a strong necessary condition for integrability of the system (1) is obtained. This new necessary condition is much stronger than that obtained in Yoshida(1987), and justifies the Painleve conjecture for the first time about the logical connection between integrability and the singular point analysis of Hamiltonian systems.

If one applies the new necessary condition to the quartic homogeneous potential,

$$V(q_1, q_2) = \frac{1}{4}(q_1^4 + q_2^4) + \frac{e}{2}q_1^2 q_2^2$$

one finds that for integrability, it is necessary that $e = 0, 1, 3$. These three cases are indeed integrable. For cubic homogeneous potential

$$V(q_1, q_2) = q_1^2 q_2 + \frac{e}{3}q_2^3$$

integrability implies $e = 1, 2, 6, 16$.

Reference

Yoshida, H. : 1987, *Physica D*, **29**, 128–142.
Yoshida, H. : 1999, *Physica D*, **128**, 53–69.
Yoshida, H. : 1999, Suuri Kagaku (Mathematical Sciences), August,